KIT
Karlsruher Institut für Technologie

Geophysical
Institute KIT-Dept. of Physics

KARLSRUHE INSTITUTE OF TECHNOLOGY

Master's thesis

Application of 2D ground-penetrating radar full-waveform inversion and comparison with borehole data

Author:

Vu Tuan Dung

First reviewer:

Prof. Dr. Thomas Bohlen

Second-reviewer:

apl. Prof. Dr. Joachim Ritter

Supervisor:

Dr. Tan Qin

A thesis submitted in fulfillment of the requirements

for the degree of Master of Science

at the KIT-Department of Physics

March 30, 2024

Declaration on oath

Ich versichere wahrheitsgemäß, die Arbeit selbstständig verfasst, alle benutzten Hilfsmittel vollständig und genau angegeben und alles kenntlich gemacht zu haben, was aus Arbeiten anderer unverändert oder mit Abänderungen entnommen wurde sowie die Satzung des KIT zur Sicherung guter wissenschaftlicher Praxis in der momentan gültigen Fassung beachtet zu haben.

I declare truthfully that I have written this thesis all by myself, that I have fully and accurately specified all auxiliary means used, that I have correctly cited (marked) everything that was taken, either unchanged or with modification, from the work of others, and that I have complied with the current version of the KIT statutes for safeguarding good scientific practice.

Karlsruhe, 2024

....

(Vu Tuan Dung)

Abstract

Ground-penetrating radar (GPR) full-waveform inversion (FWI) is an effective technique for high-resolution multi-parameter subsurface imaging. It can reconstruct dielectric permittivity and electrical conductivity models by iteratively minimizing the misfit between observed and modelled waveforms. Due to the 2D modelling cannot account for the spherical spreading of the electromagnetic waves in the 3D. Therefore, in order to implement 2D GPR-FWI for multi-offset surface GPR data, which is obtained in the field by point source, one needs a procedure to transform the observed data generated by a point source in the field to the one generated by an equivalent line source. This transformation, called the 3D-to-2D transformation, has been widely applied to seismic data, but it is quite new for multi-offset surface GPR data.

This study investigates the performance of the 3D-to-2D transformation of different waves for multi-offset surface GPR data, and its efficiency for 2D GPR-FWI. First, the effectiveness of the transformation is demonstrated by using synthetic data. After that, it is applied to multi-offset GPR field data acquired at the Rheinstetten test site in Germany. The results of 2D GPR-FWI for the field data show that the reconstructed permittivity and conductivity models are efficient in delineating the main geological feature, which is a refilled trench from the 18th century. This confirms the effectiveness of the 3D-to-2D transformation for multi-offset surface GPR data.

To evaluate the GPR-FWI results, the water content and grain size of the borehole soil samples were measured in the laboratory. I then calculated the relative dielectric permittivity from the water content using petrophysical relationships identified by the grain size. I found that the GPR-FWI result and the borehole data have a similar permittivity trend with respect to depth. This indicates that the estimated models from FWI are reliable.

Content

1. Introduction

Ground-penetrating radar (GPR) has emerged as a versatile geophysical tool in recent years, producing subsurface images. With its ability to non-destructively map and characterize subsurface structures, GPR has been widely applied in archaeology, civil engineering, environmental studies, geology, and utility detection (Lombardi et al., 2022). Generally, GPR utilizes high-frequency electromagnetic wave (EM) propagation ranging from 100 MHz to 1 GHz, transmitting the waves into the ground to obtain a high-resolution image of shallow subsurface structure at depth from a few tens of centimeters to five meters. Traditional GPR systems typically employ a single offset configuration, in which the transmitting and receiving antennas are fixed in position at a set distance. In contrast, by collecting data at various source-receiver offset distances, multi-offset surface GPR data allows for improved resolution, increased depth penetration, enhanced subsurface characterization, leading to a more accurate reconstruction of the subsurface structure, and reducing the impact of wave propagation effects (Berard et al., 2007). Compared to seismic method, GPR equipment is typically portable and relatively easy to operate, allowing for rapid deployment in the field and access to areas where seismic methods may be impractical or cost-prohibitive (Sato, 2001).

There are several methods using GPR data to interpret. Traditional approaches often involve simple methods such as reflector picking and traveltime tomography. These methods rely on identifying reflections and estimating the traveltimes of the waves to determine the depth and location of subsurface features. While these approaches have been useful for initial basic investigation where high accuracy is not required, they are limited in their ability to provide high-resolution images and accurate subsurface property estimation (Paz et al., 2017). Another alternative is full-waveform inversion (FWI), which overcomes the limitations of traditional methods and enhances the interpretation of GPR data. FWI aims to reconstruct high-resolution subsurface models by iteratively minimizing the misfit between the observed and modelled waveforms. Unlike simple picking methods, FWI takes advantage of the complete waveform information, including amplitude, phase, and frequency content, to reconstruct detailed subsurface models of electromagnetic (EM) properties (Klotzsche et al., 2019). The application of FWI to GPR data has gained significant attention in recent years. It has been successfully applied in various scenarios, including imaging buried objects, mapping geological structures, and locating subsurface utilities (Lombardi et al., 2022). However, implementation of FWI for GPR data faces certain challenges in practice due to the computational requirements involved in the inversion process, including the necessity for extensive computational resources and effective numerical algorithms. 2D GPR-FWI requires less computational effort and can be executed on a moderate computer, which is why 2D GPR-FWI is still preferred in most scenarios.

In field conditions, the wavefield is emitted by point sources, while 2D adjoint waveform inversion inherently employs line sources in a 3D environment. However, only 3D wave simulation can accurately account for the spherical propagation of

recorded waves within a 2D heterogeneous structure (Forbriger et al., 2014). Due to the expensive computational cost of the 3D approach, 2D wave propagation simulation is still preferred. To make 2D FWI applicable to field data, recorded data must be converted to equivalent waveforms as would be generated by line sources and therefore, the 3D-to-2D transformation plays an important role in 2D FWI. Such a known procedure has been applied to seismic data by Bleistein (1986) and Ursin (1990). There are some studies that have applied this transformation for multi-offset surface GPR data, namely Lavoué (2014), and Qin (2022), but the effect and efficiency of the transformation has not been shown in detail.

In this study, I simulated multi-offset surface GPR data on a 3D and 2D synthetic model to obtain two types of data. While the multi-offset GPR data simulated on a 2D synthetic model are used as reference data, those simulated on 3D model are used as input for testing the 3D-to-2D transformation. The results of the 3D-to-2D transformation which are evaluated by comparing the similarity to the reference data. The transformed data is then used as input for 2D GPR-FWI. If 2D GPR-FWI using transformed data can reconstruct models similar to those using 2D data, it will prove the efficiency of the 3D-to-2D transformation. After tested on the synthetic data, the transformation was applied to the multi-offset surface field GPR data, which was acquired in a glider field located in Rheinstetten, Germany. Previous investigations in this area have confirmed the presence of a V-shaped trench, called the Ettlinger line, which has been refilled by sediment and is now completely flattened at the surface. The GPR profile used in my study is perpendicular to the Ettlinger line, in which, I assume that the magnetic permeability is constant and equal to its value in vacuum. I performed 2D GPR-FWI on the transformed field data to obtain the relative dielectric permittivity and electrical conductivity models of the study area. The goal of 2D GPR FWI is to reconstruct models that can delineate the Ettlinger line.

To assess results of the 2D GPR-FWI mentioned above, I compare its results with in situ data at borehole locations in the study area. We know that the electrical parameters are strongly dependent on the water content of the soil (Bai et al., 2013). The apparent dielectric constant varies over a range of 3 to 40 for a change in the volumetric water content of 0 to 0.55 in soft minerals (Topp et al., 1980). Through a measurement, using time-domain reflectometry, Owenier in 2011 introduced empirical equations that provide a petrophysical relationship between dielectric permittivity value and water content. These equations which are used for different soil types, vary according to the grain size of the soil samples. I carried out a grain size measurement in the laboratory to generate a grain size distribution of the soil sample at borehole locations in the study area. Based on this, an empirical equation was selected to calculate dielectric permittivity values at the borehole locations from the water content of the soil samples measured by Qin (2022). Values of the relative dielectric permittivity models from 2D GPR-FWI then were extracted at borehole locations for a comparison with those calculated from water content of in situ data. The reliability of the FWI results increases as the similarity of the trends between them with respect to the depth increases.

2. Methodology

2.1. Forward modelling

Forward modelling describes the propagation of a wave in a given medium. In the case of GPR data, Maxwell's equations were used to describe the propagation of electromagnetic waves. Maxwell's equations are a set of fundamental equations that consist of the following equations:

Faraday's Law of electromagnetic induction

$$\nabla \times \mathbf{E} = -\frac{\partial \mathbf{B}}{\partial t} \tag{2.1}$$

Ampère's Law with Maxwell's addition

$$\nabla \times \mathbf{H} = \mathbf{J_c} + \mathbf{J_e} + \frac{\partial \mathbf{D}}{\partial t} \tag{2.2}$$

where $\mathbf{E}$ is the electric field, $\mathbf{H}$ is the magnetic field, $\mathbf{B}$ is the magnetic flux, $\mathbf{D}$ is the electric flux density. $\mathbf{J_c}$ is the conduction current density and $\mathbf{J_e}$ is the electric current sources. ∇ is the Laplace operator, $\times$ is the curl operator. The magnetic $\mathbf{B}$ and the electric flux density $\mathbf{D}$ are related to the electric field $\mathbf{E}$ and the magnetic field $\mathbf{H}$ by the constitutive relations:

$$\mathbf{B} = \mu\mathbf{H}$$
$$\mathbf{D} = \varepsilon\mathbf{E} \tag{2.3}$$

and the conduction current density is described by:

$$\mathbf{J_c} = \sigma\mathbf{E} \tag{2.4}$$

where μ is the magnetic permeability, ε is the dielectric permittivity and σ is electrical conductivity. Substituting eq. 2.3, 2.4 into eq. 2.1 and 2.2:

$$\mu\frac{\partial \mathbf{H}}{\partial t} = -\nabla \times \mathbf{E}$$

$$\sigma\mathbf{E} + \varepsilon\frac{\partial \mathbf{E}}{\partial t} + \mathbf{J}_e = \nabla \times \mathbf{H} \tag{2.5}$$

Eq. 2.5 is solved by using the finite-difference time-domain (FDTD) method of second order in time and fourth order in space. In order to absorb the outgoing waves, the convolutional perfectly matched layer was added to the model boundary. For convenience, Eq. 2.5 could be expressed in a matrix-vector formalism as follows:

$$\mathbf{M}_1\partial_t\mathbf{u} + \mathbf{M}_2\mathbf{u} - \mathbf{A}\mathbf{u} = \mathbf{s} \tag{2.6}$$

with

$$\mathbf{u} = \left(H_x, H_y, H_z, E_x, E_y, E_z\right)^T$$

$$\mathbf{s} = \left(0, 0, 0, -J_{ex}, -J_{ey}, -J_{ez}\right)^T$$

$$\mathbf{M}_1 = \begin{pmatrix} -\mu & 0 & 0 & 0 & 0 & 0 \\ 0 & -\mu & 0 & 0 & 0 & 0 \\ 0 & 0 & -\mu & 0 & 0 & 0 \\ 0 & 0 & 0 & \varepsilon_x & 0 & 0 \\ 0 & 0 & 0 & 0 & \varepsilon_y & 0 \\ 0 & 0 & 0 & 0 & 0 & \varepsilon_z \end{pmatrix}, \mathbf{M}_2 = \begin{pmatrix} 0 & 0 & 0 & 0 & 0 & 0 \\ 0 & 0 & 0 & 0 & 0 & 0 \\ 0 & 0 & 0 & 0 & 0 & 0 \\ 0 & 0 & 0 & \sigma_x & 0 & 0 \\ 0 & 0 & 0 & 0 & \sigma_y & 0 \\ 0 & 0 & 0 & 0 & 0 & \sigma_z \end{pmatrix}$$

$$\mathbf{A} = \begin{pmatrix} 0_3 & \mathbf{D} \\ \mathbf{D} & 0_3 \end{pmatrix}$$

$$\mathbf{D} = \begin{pmatrix} 0 & -\partial_z & \partial_y \\ \partial_z & 0 & -\partial_x \\ -\partial_y & \partial_x & 0 \end{pmatrix} = \mathbf{D}_1\partial_x + \mathbf{D}_2\partial_y + \mathbf{D}_3\partial_z, \ \mathbf{D}_i^* = \mathbf{D}_i^T = -\mathbf{D}_i$$

$$\mathbf{D}_1 = \begin{pmatrix} 0 & 0 & 0 \\ 0 & 0 & -1 \\ 0 & 1 & 0 \end{pmatrix}, \mathbf{D}_2 = \begin{pmatrix} 0 & 0 & 1 \\ 0 & 0 & 0 \\ -1 & 0 & 0 \end{pmatrix}, \mathbf{D}_3 = \begin{pmatrix} 0 & -1 & 0 \\ 1 & 0 & 0 \\ 0 & 0 & 0 \end{pmatrix}, \mathbf{D}^T = \mathbf{D}$$

$$\mathbf{D}^* = (\mathbf{D}_i\partial_i)^* = -\mathbf{D}_i^*\partial_i = \mathbf{D}_i\partial_i = \mathbf{D} => \mathbf{A}^* = \mathbf{A}$$

where 0_3 is the 3x3 zero matrix. The superscript * is the transpose conjugate operator and for the real values, it is simple transpose operator ^{T}. $\partial_1 = \partial_x, \partial_2 = \partial_y, \partial_3 = \partial_z$.

2.2. 3D-to-2D transformation

Following Forbringer et al. (2014), the far field single-wavenumber transformation factor $F_{-D}(r, k)$ has proven useful in several contexts.

$$F_{-D}(r, k) = \sqrt{\frac{2\pi r}{k}} e^{i\pi/4} C \tag{2.7}$$

where r is the propagation distance, k is the wavenumber for the angular frequency ω. Assuming that the phase velocity $v_{ph} = \omega/k$ is a unique quantity when discussing propagating waves, we obtain the single-velocity transformation factor:

$$F_{-D} = \underbrace{\sqrt{2rv_{ph}}}_{F_{amp}} \underbrace{\sqrt{\frac{\pi}{\omega}} e^{i\pi/4} C}_{\tilde{F}_{\sqrt{t^{-1}}}} \tag{2.8}$$

where $\tilde{F}_{\sqrt{t^{-1}}}$ is a phase factor independent of offset or wave velocity, $C = 1 \ m^{-1}$ is a factor that we add on when defining a line source as force density extending infinitely in y-direction. The phase factor can be applied to any component of the wavefield in the same way. It can be applied in the Fourier domain by multiplication with $\tilde{F}_{\sqrt{t^{-1}}}(\omega)$ or in the time domain by convolution with

$$F_{\sqrt{t^{-1}}}(t) = \begin{cases} \dfrac{1}{\sqrt{t}} & \text{if } t \geq 0 \text{ and} \\ 0 & \text{otherwise} \end{cases} \tag{2.9}$$

The amplitude factor $F_{amp} = \sqrt{2rv_{ph}}$ is frequency independent and can be applied in the Fourier domain or time domain equally. It depends only on the propagation distance r and the phase velocity v_{ph}.

For an impulse source and transient body waves, the propagation distance $r = tv_{ph}$ can be estimated form the velocity v_{ph} and the wave's traveltime t which is equal to the arrival time if the wave was excited at $t = 0$. Then the amplitude factor in eq. (2.8) becomes

$$F_{amp}(t) = v_{ph}\sqrt{2t} \tag{2.10}$$

This factor is derived by Ursin (1990) using asymptotic ray theory for reflected waves and so-called the reflected-wave transformation.

In the case of direct wave, the offset r_{offset} is identical to the propagation distance r, hence, we can estimate the phase velocity:

$$v_{ph} = \frac{r_{offset}}{t} \tag{2.11}$$

then the amplitude factor in eq. (2.8) becomes

$$F_{amp}(t) = \sqrt{2r_{offset}\frac{r_{offset}}{t}} = r_{offset}\sqrt{\frac{2}{t}} \tag{2.12}$$

this is called direct-wave amplitude factor.

2.3. Full-waveform inversion

The basic concept of the FWI is to find a model of the subsurface that describes the observed data. This is done by iterating until the misfit between the synthetic data and the observed data is minimized. The FWI uses the full waveforms including wave amplitude and phase to find the best fitting model, so it can achieve a resolution below the size of a wavelength. However, wave propagation is a non-linear quantity, therefore, FWI is also a non-linear problem as well.

Misfit function

The misfit in my study is quantified by the L_2 -norm.

$$\Phi(\mathbf{m}) = \frac{1}{2}\|\mathbf{d}_{syn} - \mathbf{d}_{obs}\|_2^2 = \frac{1}{2}\|R(\mathbf{u}(\mathbf{m}) - \mathbf{d}_{obs}\|_2^2 \tag{2.13}$$

Eq (2.13) indicates the residual between the synthetic data $\mathbf{d}_{syn}$ and the observed data $\mathbf{d}_{obs}$, in which, the synthetic data are extracted from the forward wavefield $\mathbf{u}$ by a restriction operator R.

To minimize the misfit function Φ, an iterative process was carried out by a gradient-base algorithm with a starting model $\mathbf{m}_0$ until the minimum of it is reached. A general rule for iteratively updating model $\mathbf{m}$ is to minimize misfit Φ as follows.

$$\mathbf{m}_{n+1} = \mathbf{m}_n - \alpha \Delta \mathbf{m}_{n+1} \tag{2.14}$$

$$\Delta \mathbf{m}_{n+1} = -\mathbf{P}\frac{\partial \Phi}{\partial \mathbf{m}} + \gamma \Delta \mathbf{m}_n \tag{2.15}$$

where $\mathbf{m}_{n+1}$ and $\mathbf{m}_n$ are the model at $(n+1)$th and nth iteration, α is the step length that defines how much the model parameters can change in one iteration step. In eq (2.15), γ is the scaling factor (Polak and Ribiere, 1969) and $\mathbf{P}$ is the preconditioner (Plessix and Mulder, 2004). In order to compute $\Delta \mathbf{m}_{n+1}$ for the $(n+1)$th iteration, the conjugated-gradient method was used.

During the inversion, if the relative misfit value is greater than the stop criterion, the inversion goes on to the next stage and the residual wavefields are backpropagated.

Due to the non-linear nature of the forward problem, which involves applying a non-linear operator to the synthetic data output, the misfit function Φ is also non-linear. Consequently, the potential issue arises where the problem may converge to a local minimum rather than a global minimum. To avoid this problem, a multi-stage approach can be used. This approach consists of several stages, each representing a complete FWI workflow that is executed sequentially, with each stage building upon the model results obtained from the previous stage. However, each stage operates within a different frequency range. Initially, lower frequencies are employed to smooth the misfit function and facilitate convergence towards the global minimum. Subsequently, higher frequencies are introduced in subsequent stages. Figure 2.1 (Bunks et al., 1995) illustrates the objective functions at different frequency scales. It is important to note that as the frequency increases, the likelihood of the misfit function becoming trapped in a local minimum increase.
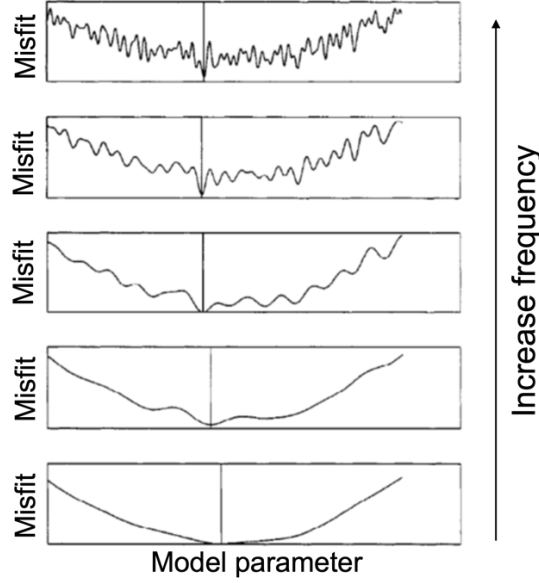
Figure 2.1 Objective functions at different scale lengths by Bunks et al. (1995). The top is more complex due to a higher frequency, thus filled with more local minimum.

Adjoint state method

The gradient of the misfit function is calculated by the adjoint method (Plessix, 2006). Augmented functional used in the 1st order adjoint method is:

$$L_1(\mathbf{m}, \mathbf{u}, \mathbf{u}_1) = \Phi(\mathbf{u}) + \langle \mathbf{u}_1, F(\mathbf{u}, \mathbf{m}) \rangle_w \tag{2.16}$$

where

$$F(\mathbf{u}, \mathbf{m}) = \mathbf{M}_1 \partial_t \mathbf{u} + \mathbf{M}_2 \mathbf{u} - \mathbf{A}\mathbf{u} - \mathbf{s} = 0$$

$$\mathbf{m} = (\varepsilon, \sigma, \mu)^T, \mathbf{u}|_{t=0} = 0, \mathbf{u}|_{x \in \partial\Omega} = 0 \tag{2.17}$$

With Ω is the spatial computation domain and the inner product $\langle \mathbf{h}_1, \mathbf{h}_2 \rangle_w$ in domain $W = \Omega \times [0, \mathrm{T}]$ is defined by

$$\langle \mathbf{h}_1, \mathbf{h}_2 \rangle_w = \int_0^{\mathrm{T}} \int_\Omega \mathbf{h}_1^*(x, t) \mathbf{h}_2(x, t) dt dx \tag{2.18}$$

For any $\mathbf{u}_1$:

$$L_1(\mathbf{m}, \mathbf{u}, \mathbf{u}_1) = \Phi(\mathbf{u}) \tag{2.19}$$

The augmented functional could be rewritten:

7

$$L_1(\mathbf{m}, \mathbf{u}, \mathbf{u_1}) = \frac{1}{2}\int_0^T \int_\Omega (R\mathbf{u} - \mathbf{d}_{obs})^2 dt dx + \int_0^T \int_\Omega \mathbf{u}_1^*(\mathbf{M}_1 \partial_t \mathbf{u} + \mathbf{M}_2 \mathbf{u} - A\mathbf{u}$$
$$- \mathbf{s})dt dx \tag{2.20}$$

If the final condition and boundary condition of $\mathbf{u}_1$ are satisfied by

$$\mathbf{u}_1|_{t=0} = 0, \mathbf{u}_1|_{x\in\partial\Omega} = 0 \tag{2.21}$$

Do integration by parts, then the augmented functional is:

$$L_1(\mathbf{m}, \mathbf{u}, \mathbf{u_1}) = \frac{1}{2}\int_0^T \int_\Omega (R\mathbf{u} - \mathbf{d}_{obs})^2 dt dx + \int_0^T \int_\Omega (-\mathbf{M}_1 \partial_t \mathbf{u_1})^* \mathbf{u} + (\mathbf{M}_2 \mathbf{u_1})^* \mathbf{u}$$
$$- (A\mathbf{u_1})^* \mathbf{u} - \mathbf{u}_1^* \mathbf{s}] dt dx \tag{2.22}$$

where

$$\mathbf{M}_1^* = \mathbf{M}_1, (\mathbf{M}_1 \partial_t)^* = -\mathbf{M}_1^* \partial_t = -\mathbf{M}_1 \partial_t, \mathbf{M}_2^* = \mathbf{M}_2$$

$$\mathbf{D}^* = (\mathbf{D}_i \partial_i)^* = -\mathbf{D}_i^* \partial_i = \mathbf{D}_i \partial_i = \mathbf{D} => A^* = A \tag{2.21}$$

which is derived from the initial, final and boundary condition in Eq. 2.17 and 2.21 (Yang et al., 2016).

Derivative with respect to $\mathbf{u}$, then we get:

$$\frac{\partial L_1}{\partial \mathbf{u}} = \int_0^T \int_\Omega (R(R\mathbf{u} - \mathbf{d}_{obs}) - \mathbf{M}_1 \partial_t \mathbf{u}_1 + \mathbf{M}_2 \mathbf{u}_1 - A\mathbf{u}_1)^* dt dx \tag{2.23}$$

To satisfy the final condition of $\mathbf{u}_1$ in Eq. 2.21, the time needs to be reversed by substituting $t' = T - t$ with $\partial_{t'} = -\partial_t, dt' = -dt$ in the Eq. 2.23

$$\frac{\partial L_1}{\partial \mathbf{u}} = -\int_0^T \int_\Omega (R^*(R\mathbf{u} - \mathbf{d}_{obs}) + \mathbf{M}_1 \partial_{t'} \mathbf{u}_1 + \mathbf{M}_2 \mathbf{u}_1 - A\mathbf{u}_1)^* dt' dx \tag{2.24}$$

By making $\frac{\partial L_1}{\partial \mathbf{u}} = 0$, the self-adjoint equation is:

$$\mathbf{M}_1 \partial_{t'} \mathbf{u}_1 + \mathbf{M}_2 \mathbf{u}_1 - A\mathbf{u}_1 = -R^*(R\mathbf{u} - \mathbf{d}_{obs})$$

$$\mathbf{u}_1 = \left(H_{1x}, H_{1y}, H_{1z}, E_{1x}, E_{1y}, E_{1z}\right)^T \tag{2.25}$$

And the wavefield residual $R^*(R\mathbf{u} - \mathbf{d}_{obs})$ is used as the sources for back propagation. The 1st order adjoint equation is:

$$\mathbf{u}_1: \begin{cases} -\mu\dfrac{\partial \mathbf{H}_1}{\partial t'} - \nabla \times \mathbf{E}_1 = -R^*(R\mathbf{H} - \mathbf{H}_{obs}) \\ \varepsilon\dfrac{\partial \mathbf{E}_1}{\partial t'} + \sigma\mathbf{E} - \nabla \times \mathbf{H}_1 = -R^*(R\mathbf{E} - \mathbf{E}_{obs}) \end{cases} \tag{2.25}$$

Derivative with respect to model parameter $\mathbf{m}$ from Eq. 2. 20:

$$\nabla\Phi(\mathbf{m}) = \frac{\partial\Phi}{\partial\mathbf{m}} = \frac{\partial L_1}{\partial\mathbf{m}} = \int_0^T \mathbf{u}_1^* \left(\frac{\partial\mathbf{M}_1}{\partial\mathbf{m}}\partial_t\mathbf{u} + \frac{\partial\mathbf{M}_2}{\partial\mathbf{m}}\mathbf{u}\right) dt \tag{2.26}$$

And the gradient of objective function respect to the electrical parameters are:

$$\frac{\partial\Phi}{\partial\varepsilon} = \int_0^T \left(E_{1x}\frac{\partial E_x}{\partial t} + E_{1y}\frac{\partial E_y}{\partial t} + E_{1z}\frac{\partial E_z}{\partial t}\right) dt$$

$$\frac{\partial\Phi}{\partial\sigma} = \int_0^T (E_{1x}E_x + E_{1y}E_y + E_{1z}E_z)dt \tag{2.27}$$

Subset full-waveform inversion (SFWI)

Subset full-waveform inversion is a study of FWI that was tested and applied by Qin (2022). In which, computational cost is reduced by using the data simulated on a subset model to approximate the data simulated on an entire model. Due to the high attenuation of EM waves propagating in the subsurface, the energy of the reflected waves will be lower than the noise level when the distance between the transmitter and receiver exceeds a certain value, and therefore, the size of the subset model can be much smaller than the original model. The subset model mi can be extracted from the original model.

$$\mathbf{m}_i = \mathbf{A}_i\mathbf{m} \tag{2.28}$$

where $\mathbf{A}_i$ is a matrix for transformation with size of $n_{mi} \times n_m$. n_m and n_{mi} are the size of original model $\mathbf{m}$ and extracted model $\mathbf{m}_i$, respectively. In each row of matrix $\mathbf{A}_i$, there are n_{m-i} zeros and only one value one corresponding to the coordinate index of one grid in $\mathbf{m}_i$. Therefore, this matrix is highly sparse. And the misfit function of subset model $\mathbf{m}_i$ is:

$$\Phi(\mathbf{m}_i) = \sum_{i=1}^{n_s} \Phi_i(\mathbf{m}_i), \quad \Phi_i(\mathbf{m}_i) = \frac{1}{2}\left\|\mathbf{d}_i^{syn}(\mathbf{m}_i) - \mathbf{d}_i^{obs}\right\|_2^2 \tag{2.29}$$

where $\mathbf{d}_i^{syn}(\mathbf{m}_i)$ is the data obtained by simulating the EM wavefield on extracted model $\mathbf{m}_i$ with the same acquisition of original model $\mathbf{m}$. Using the adjoint state method to calculate the gradient of the subset model $\partial\Phi_i(\mathbf{m}_i)/\partial\mathbf{m}$ and form a padded gradient $\partial\Phi_i(\mathbf{m}_i)/\partial\mathbf{m}$ by transforming the subset gradient back to its position in the original model as follows:

$$\frac{\partial\Phi_i(\mathbf{m}_i)}{\partial\mathbf{m}} = \mathbf{A}_i^{\mathrm{T}}\frac{\partial\Phi_i(\mathbf{m}_i)}{\partial\mathbf{m}_i} \tag{2.30}$$

where superscript ^{T} is the transpose operator. The most important assumption in SFWI is that the data $\mathbf{d}_i^{syn}(\mathbf{m}_i)$ of the ith source simulated from the extracted model $\mathbf{m}_i$ equal data $\mathbf{d}_i^{syn}(\mathbf{m})$ obtained from the original model $\mathbf{m}$.

$$d_i^{\text{syn}}(\mathbf{m}) \approx d_i^{\text{syn}}(\mathbf{m}_i) \qquad (2.31)$$

As a consequence, $\Phi_i(\mathbf{m}_i) \approx \Phi_i(\mathbf{m})$, $\Phi(\mathbf{m}_i) \approx \Phi(\mathbf{m})$ and $\partial\Phi(\mathbf{m})/\partial\mathbf{m} \approx \partial\Phi(\mathbf{m}_i)/\partial\mathbf{m}$. In this case, an approximation is that:

$$\frac{\partial\Phi(\mathbf{m})}{\partial\mathbf{m}} \approx \sum_{i=1}^{n_s} \frac{\partial\Phi_i(\mathbf{m}_i)}{\partial\mathbf{m}} \qquad (2.32)$$

In the 2D case since that $\mathbf{m}$ and $\mathbf{m}_i$ have the same length in z direction (Cartesian coordinate system), we have the speedup factor $S_{2D}^x = n_x/n_{xi}$, where n_x and n_{xi} are the lengths of $\mathbf{m}$ and $\mathbf{m}_i$ in x direction (Qin, 2022).

2.4. Grain size measurement

Grain size measurement was carried out in the laboratory to determine the grain size of soil samples from two boreholes in my study. Based on the grain size distribution, I can choose an appropriate petrophysical relationship between permittivity and water content for my field survey data to calculate the dielectric permittivity at borehole locations. And then, these results could be used to evaluate the GPR-FWI results of the field GPR data.

This sieve analysis method was performed to determine the grain size distribution of soil samples larger than 0.063 mm in diameter. It is commonly used for sand and gravel but cannot be used as the sole method for determining the grain size distribution of finer soils (Hossain et al.,2021). The sieves used in this method, which are made of woven wires with square openings are shown in Figure 2.2. In this study, we assume that a particle smaller than 0.063 mm is one class and particles larger than 2 mm belong to another class. Therefore, our soil sample is classified into 8 classes based on the aperture size of the sieves as shown in Table 2.1.

Table 2.1 Sieve size use to classified soil sample.

No.	Opening (mm)
1	2
2	1
3	0.63
4	0.5
5	0.2
6	0.125
7	0.63

Figure 2.2 Sieves are used in the grain size measurement.

Due to this measurement, soil samples will be dried in the oven before weighing each grain-sized class, water content measurement of samples must be carried out to make sure that there is no error due to the weight of water content in the soil sample. And then, the soil sample will be sieved through a set of sieves as mentioned above. The retained particles in each sieve are dried in an oven before being weighted. We then can calculate the percentage of each class.

$$\% \, Retained_i = \frac{w_{sieve\_i}}{w_{total}} \times 100\% \tag{2.46}$$

where w_{total} is mass of one sample, w_{sieve_i} is the mass of sample retained in sieve class ith. The next step is to find the cumulative percentage of aggregate retained in each sieve. To do this, add up the total amount of aggregate that is retained in each sieve to the amount retained in the previous sieves.

$$\% \, Cumulative\_Retained_i = \sum_{1}^{7} \% \, Retained_i \tag{2.47}$$

These values are then plotted on a graph with cumulative percent retained on the y axis and logarithmic sieve size on the x axis as shown in Figure 2.3. From this curve, we can understand the behavior of the soil. As the grain size decreases, the electrical permittivity tends to increase (Gomaa, 2022), a correlation with other physical properties namely electrical permittivity, conductivity could be generated.
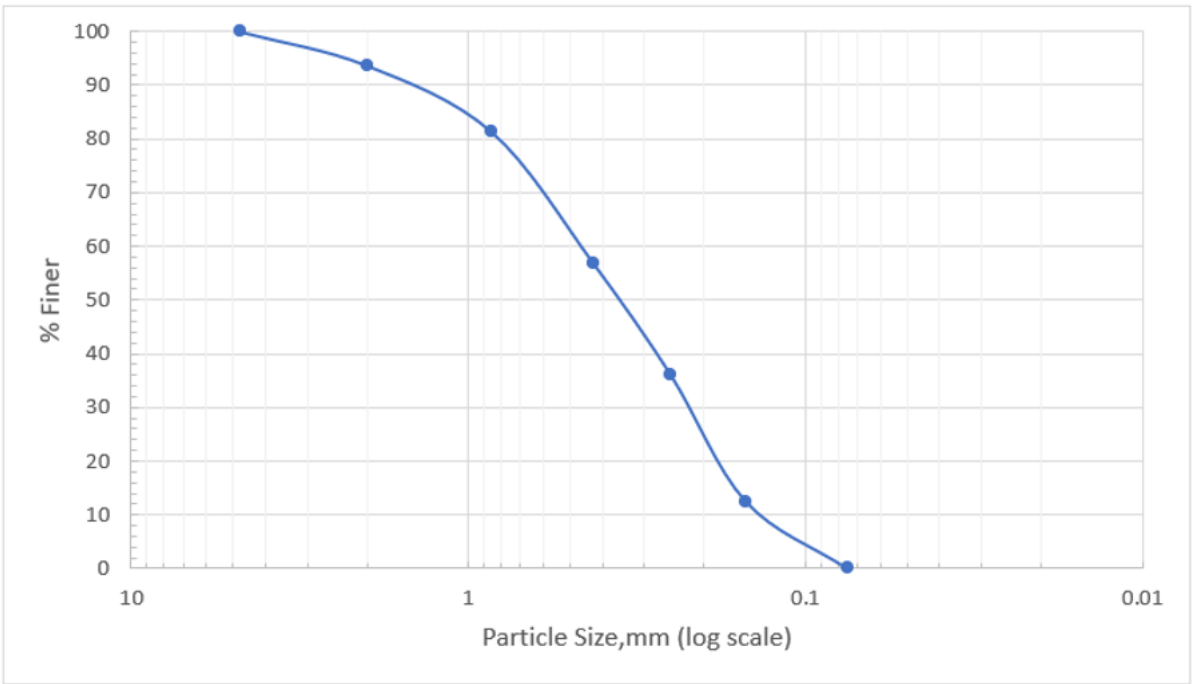
Figure 2.3 Distribution curve of grain size.

3. Validity of spreading transformation

3.1. Synthetic data

Setting

Figure 3.1 shows the workflow of the synthetic test. A set of 2D synthetic models of electrical conductivity σ, dielectric permittivity ε and magnetic permeability μ were generated with a grid size of Nx/Ny is 1130/175. The grid spacing for all spatial directions is 0.04 m. The time of wave propagation is 163 ns with a time temporal sampling of 0.05 ns. In which, the magnetic permeability model maintains a constant value and is equal to its value in vacuum, while the electrical conductivity and dielectric permittivity models consist of three layers with two interfaces at 2 m and 4 m in depth. A triangle abnormally embedded below the ground, in the middle models to resemble the Ettlinger trench located in the air glider field where our field test site will be carried out. Another set of 3D synthetic models which was also generated based on the above 2D models, was uniformly extended in the third spatial dimension (Figure 3.2) with Nx/Ny/Nz is 1130/175/30 grid points.

I applied a "walk-away" method to acquire multi-offset surface GPR data on one side of the source. In this study, the acquisition configuration includes 18 sources generating the transverse magnetic wave (only one electric field component perpendicular to the survey plane), and 192 receivers were used in each of source to record GPR data from 0.3 to 8.0 m offset (Due to strong attenuation of electromagnetic wave, this distance is optimization for FWI results and computation timing). The wavelet is a 100 MHz shifted Ricker wavelet. I computed wavefields excited by point and line sources, respectively, using 3D and 2D finite difference forward modelling in the time domain to obtain 3D- and 2D- radargrams. Boundary reflections are reduced by a convolutional perfectly matched layer (CPML) that is set to be 10 grids.
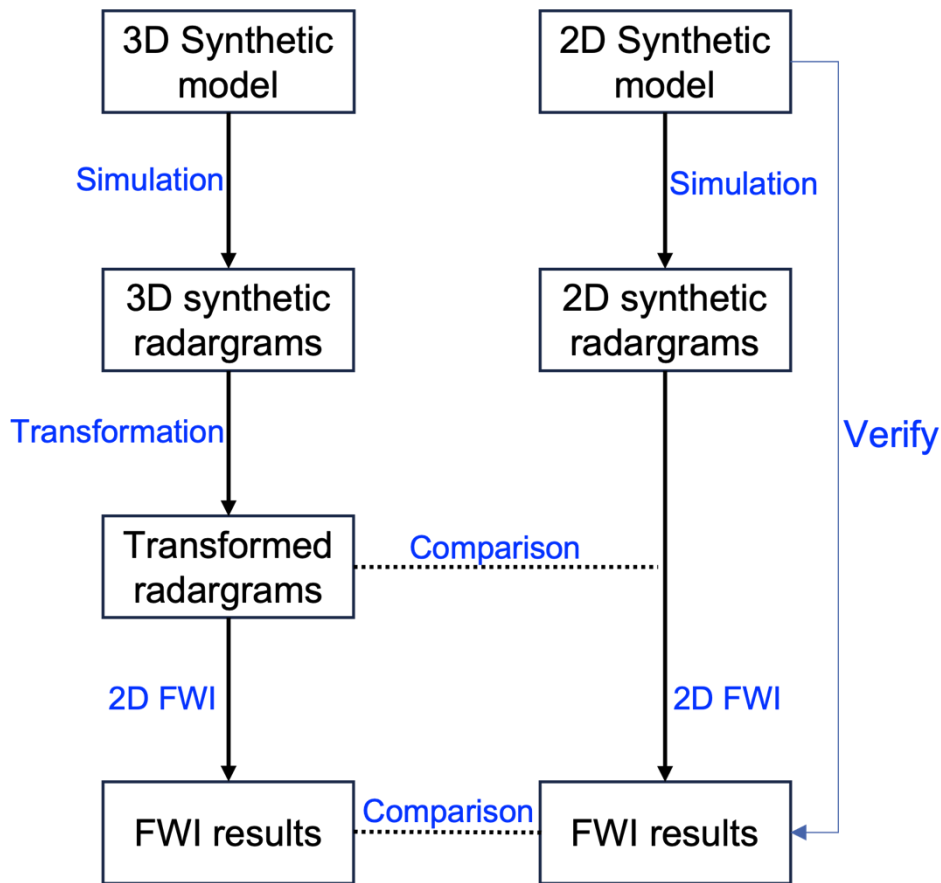
Figure 3.1 Workflow of the synthetic data testing

2D radargrams are used as input for FWI, while 3D radargrams are converted to line source radargrams by 3D-to-2D transformation. During this step, 3D-to-2D transformations will be tested to generate various sets of transformed radargrams, which will serve as input for the subsequent 2D GPR-FWI. In order to facilitate a comparison between FWI results obtained from 2D data and 3D-to-2D transformed data, the parameters in FWI configurations remain completely the same.

For initial models, I've created gradient models where the relative dielectric permittivity increases from 8.5 at the top to 20 at the bottom, while the electrical conductivity decreases from 3 to 1 nS/m.
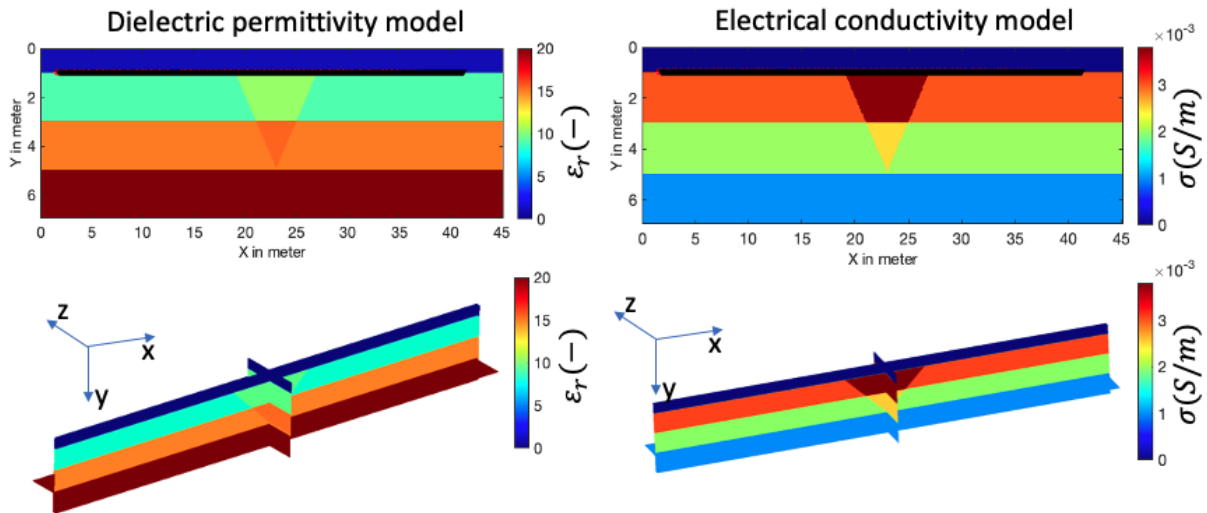
Figure 3.2 2D synthetic models (Top) and 3D synthetic models (Bottom) of relative dielectric permittivity and electrical conductivity.

I employed a multiscale strategy in the inversion to avoid circle skipping and selected five inversion stages to invert the data with progressively expanding bandwidth and decreasing wavelength (Meles et al., 2012). From the first stage to the fifth stage, the frequency bands expand from 5 – 30, 50, 80, 100 and 120 MHz, respectively. The maximum iteration in each stage is 15, and the stopping criterion is that the relative data misfit improvement is less than 1 percent. An estimated wavelet correction is filtered by stabilized deconvolution and used to correct the source time function at the beginning of each stage (Gross et al., 2014). For the known air layer, I multiplied the gradient by a taper to zero out the gradient in this layer.

Results

Figure 3.3 shows the normalized radargrams of the 1st source simulated on the 2D model. The data contains the air wave which has highest velocity, the ground wave and the waves reflected from two interfaces.

Figure 3.4 shows the wave field excited by the original line and point sources. The radargrams are normalized to their maximum amplitude, therefore, the amplitude decay with offset is not apparent, and we cannot compare the true amplitude. However, the wavefields excited by a point source are advanced in phase with respect to the wavefield excited by a line source. For a shot at the 1.56 m profile location (very left part of the model), we observed the reflected wave from the first boundary with a lower phase velocity than for that at profile location of 21.64 m. The reason for the difference is that due to the abnormal triangle in the middle model with higher permittivity and conductivity.
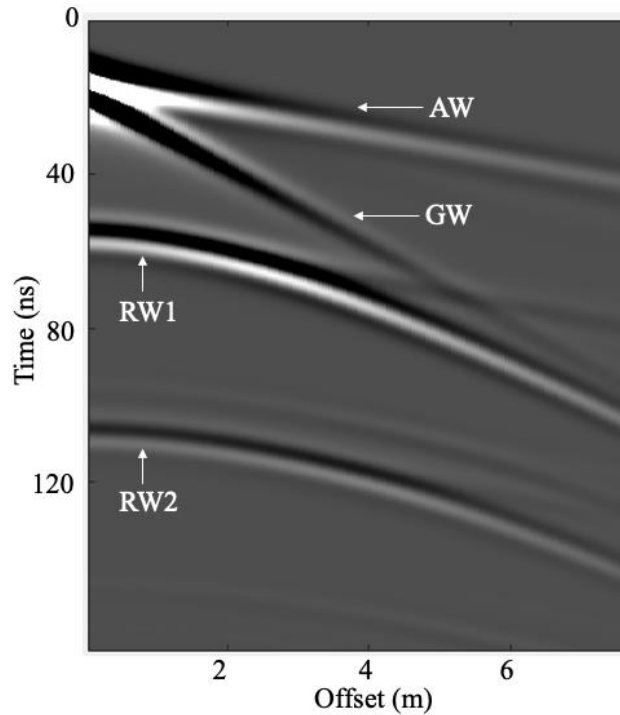
Figure 3.3 Radargrams of the 1st source shows the air wave (AW), ground wave (GW), reflected wave from the first interface (RW1) and reflected wave from the second interface (RW2) in the synthetic model.

Figure 3.5(a) and 3.5(b) display the amplitude factor of the single velocity transformation and the reflected wave transformation, where a taper was applied at the top to zero out the area without any useful information. For a given offset, the amplitude factor of the first transformation is a constant value. It should be noted that the amplitude factor of the reflected wave transformation will vary with depth (time).

Figure 3.6 shows a comparison of line source and transformed point source radargrams with single-velocity transformation. Traces are not normalized, but the amplitudes are scaled to the amplitude of the line source radargrams. This transformation reproduces the phases of waves quite well. However, for the amplitude, there are some differences between line source data and transformed data due to this transformation simplifies the model by assuming that the phase velocity $v_{ph} = \omega/k$ is a unique quantity when discussing wave propagation, and therefore, the amplitude factor of this transformation varies with the offset. Indeed, the amplitude factor of this transformation is good only for reflected waves from the second interface, while it is not suitable for the other waves.
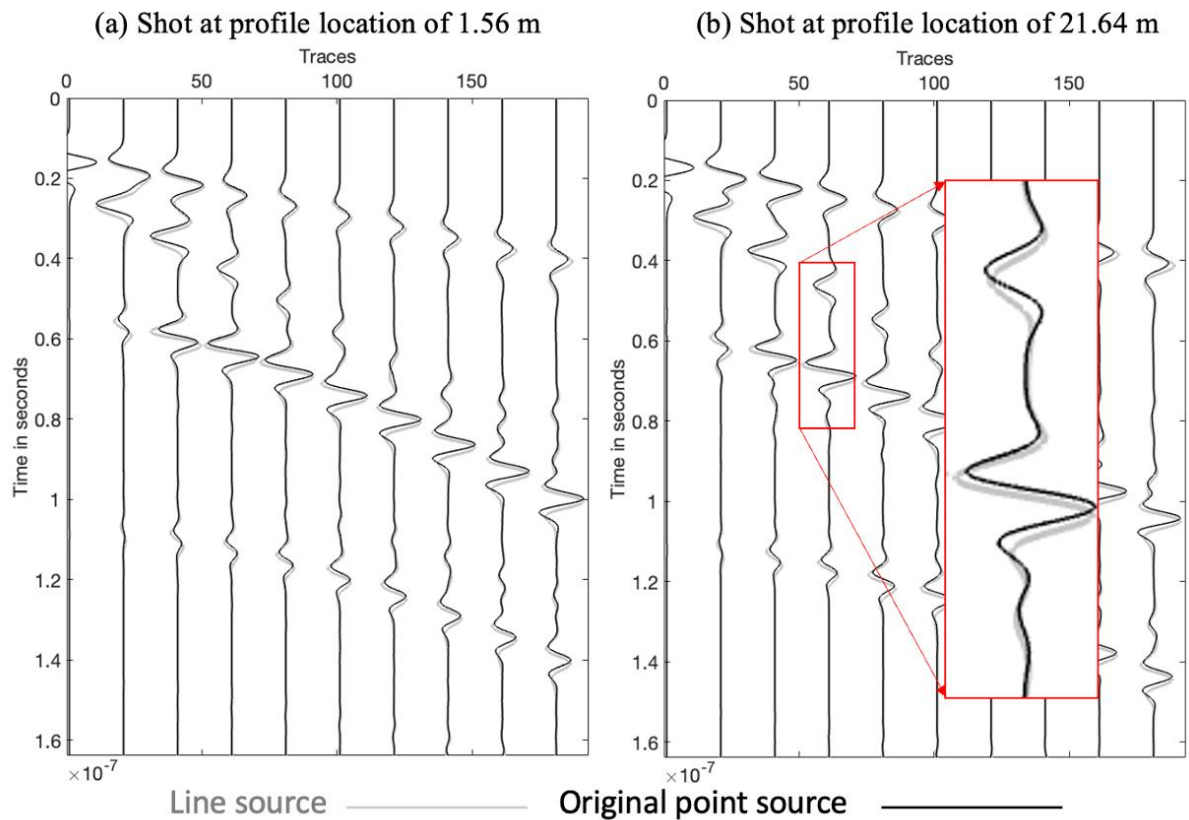
Figure 3.4 Comparison of line source seismograms and point source radargrams for the models in Figure 3.2, only every 20th trace is displayed. Radargram (a) shows a shot at profile location of 1.56 m (very left part of the model), radargram (b) of 21.64 m (middle of the model). The radargrams are trace normalized otherwise comparison would not be possible due to different decay of amplitudes.

Figure 3.7 shows the comparison between line source and transformed point source radargrams with reflected wave transformation. It indicates a good match not only in phase but also in amplitude, especially when looking at the red zoom-in box in Figure 3.7 the difference between line source and transformed point source radargrams in case of the single velocity was significantly improved in this case. In this , we consider that the amplitude factor of the reflected wave transformation increases with increasing of traveltime and velocity, as shown in Figure 3.5(b). Therefore, it is not match for the air waves.

17
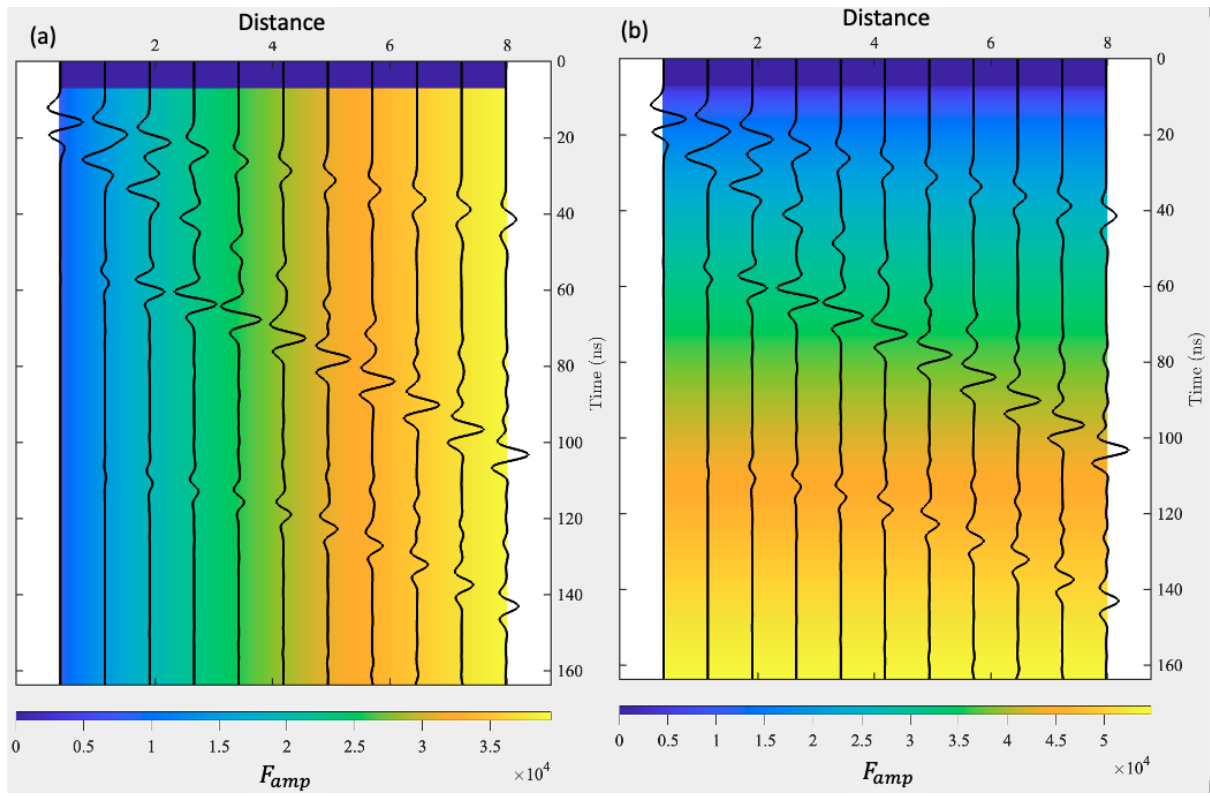
Figure 3.5 Amplitude factor of the single velocity transformation (a) and reflected wave transformation (b).
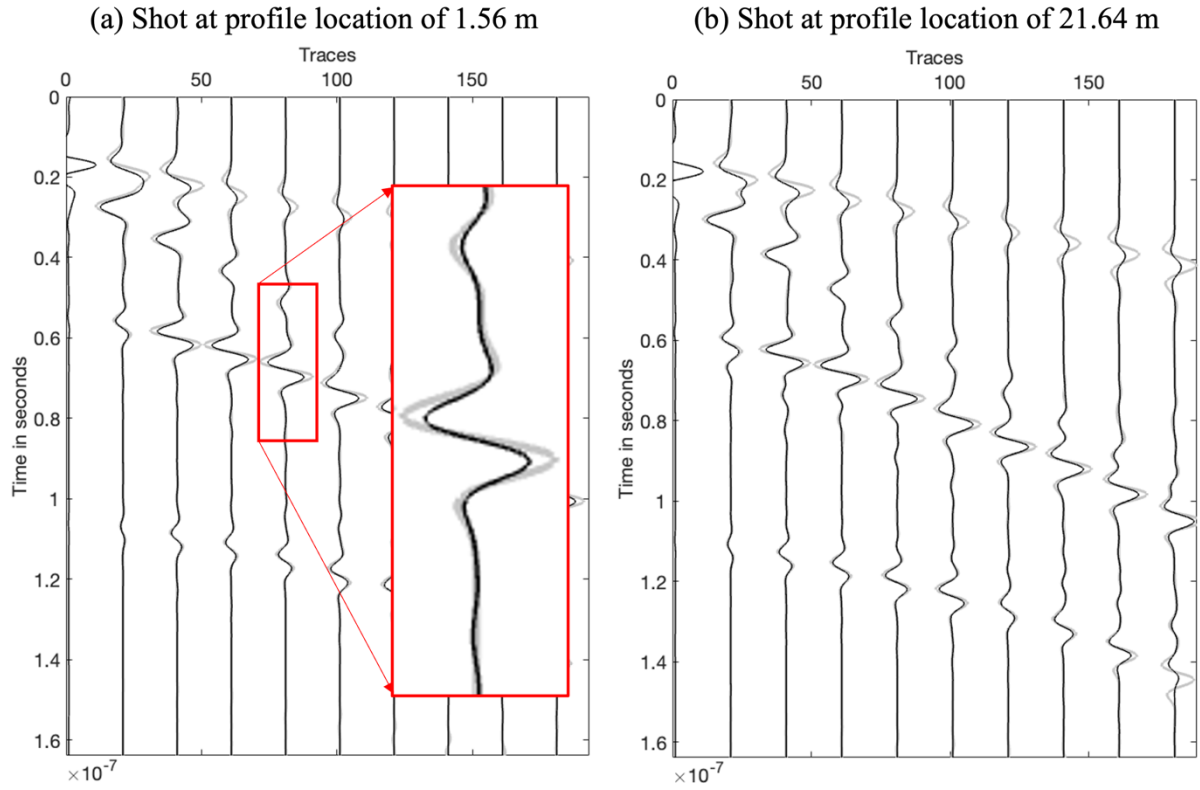
Figure 3.6 Result of single velocity transformation for the 3D data: Comparison of line source radargrams and transformed point source radargrams with the single velocity transformation for the true 3D model in Figure 3.2; only every 20th trace is displayed. Radargram (a) shows a shot at profile location of 1.56 m (very left-hand part of the model), Radargram b) of 21.64 m (middle of the model). The radargrams are scaled to the amplitude of line source radargrams.

In order to obtain a reference FWI result, I used line source radargrams calculated by a 2D solver as observed data. The objective is to find a reference to the optimal resolution obtained by FWI of the test structure. Then, all FWI results of transformed point source data are compared with this 2D FWI result. In the following, the FWI results of line source data will be referred as the reference inversion. In this study, I assume that the magnetic permeability is constant and equal to its value in vacuum. Therefore, only two parameters are considered: relative dielectric permittivity and electrical conductivity.

In Figure 3.2 and Figure 3.8 the true subsurface and the FWI initial models are plotted, respectively. Figure 3.9 shows the comparison between radargrams excited by the true line source and the reconstructed model. The FWI results are quite consistent with the observed data in both phase and amplitude. There are some differences in the far offset traces of the reflected waves from the first interface. It means that with this configuration of FWI, for the far offset, the results of FWI could not match with the observed data. This may be the reason for the poor far-offset matching between the reference and transformed data in the following.
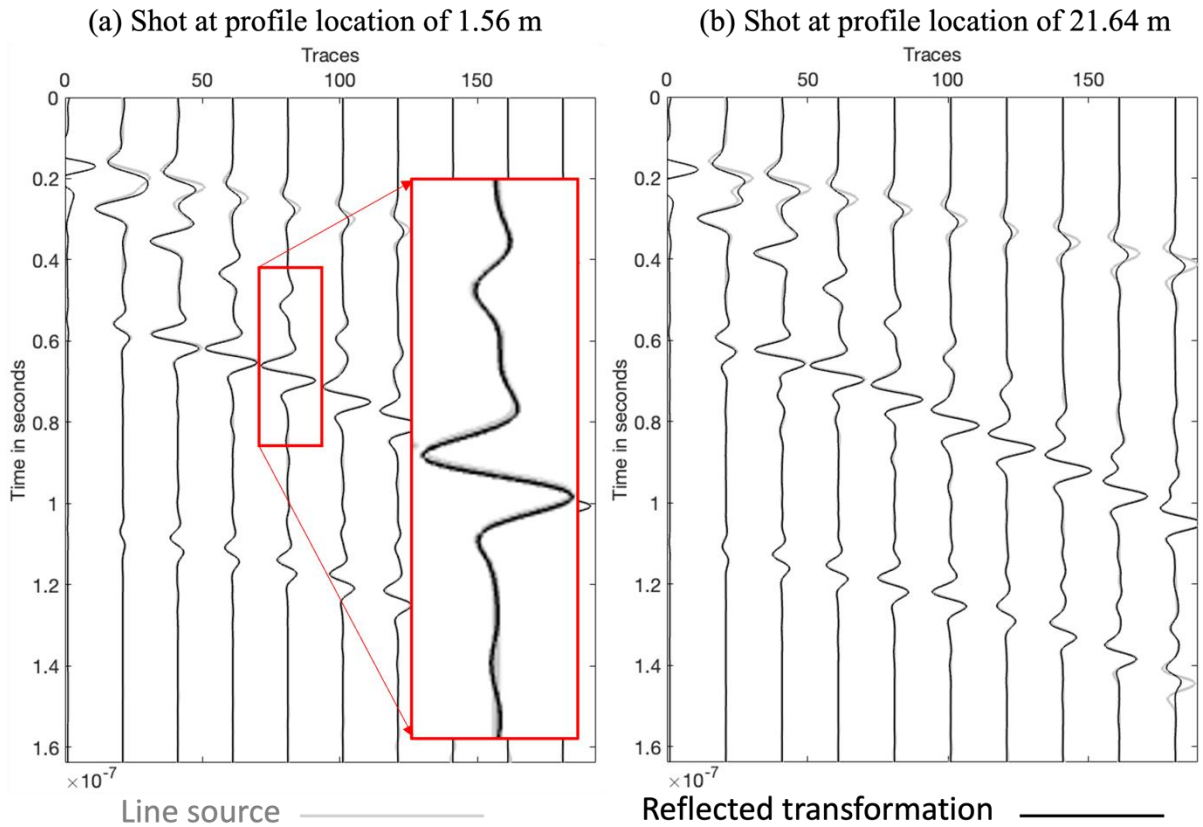
(a) Shot at profile location of 1.56 m

(b) Shot at profile location of 21.64 m

Line source

Reflected transformation

Figure 3.7 Result of reflected wave transformation for the 3D data: Comparison of line source radargrams and transformed point source radargrams with the reflected wave transformation for the true 3D model in Figure 3.2; only every 20th trace is displayed. Radargram (a) shows a shot at profile location of 1.56 m (very left-hand part of the model), Radargram b) of 21.64 m (middle of the model). The radargrams are normalized to the amplitude scale of line source radargrams.
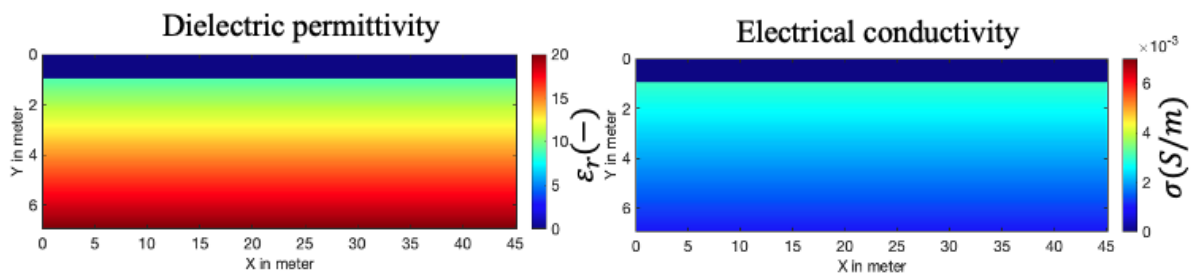
Figure 3.8 Layered initial model for reconstruction tests. Left model displays the dielectric permittivity model, right model is electrical conductivity.
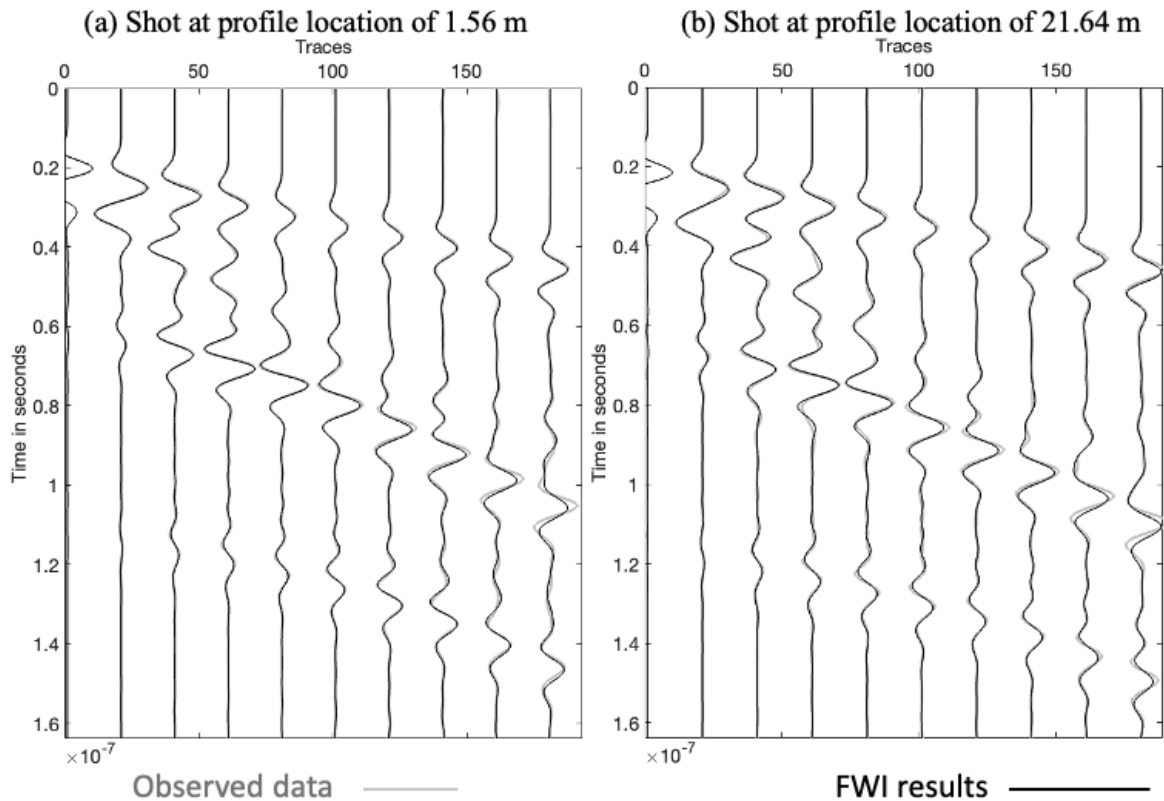
Figure 3.9 Result of reference inversion: comparison of observed data and inversion results of true line source radargrams as observed data; only every 20th trace is displayed. Radargrams (a) show a shot at profile location of 1.56 m (very left-hand part of the model), radargrams (b) of 21.64 m (middle of the model). The radargrams are trace normalized to the amplitude scale of observed data, therefore we can compare amplitude between them.

In Figure 3.10, the FWI results for the dielectric permittivity and electrical conductivity are plotted with the same color bar in Figure 3.2 and 3.8. The permittivity model can delineate the upper part of the triangular trench and the interfaces between the three horizontal layers. It is difficult to recognize the lower part of the trench by the FWI results. Due to the lack of long wavelength information in the surface multi-offset GPR data, the absolute values of these geological events are not reliable (Lavoué et al., 2014). In addition, the difference in electrical values between the inner and outer V-shaped trench is not large enough, which is the reason why our FWI results cannot separate the bottom of the trench from the background field. Looking at the conductivity model, there are more artifacts compared to the permittivity model, such as in the first layers. At the location of the trench, it indicates some different values compared to the neighboring ones, but it is not clear to define the shape of the trench. Therefore, in the scope of work of this study, it can be said that conductivity model estimation is more difficult to reconstruct.

I also do the same configuration of 2D FWI for the point source data to make a comparison. The true models and initial models remain the same. Figure 3.11 displays the FWI results for the point source data. We cannot recognize any interface, while the

21

upper part of both models contains mainly artifacts. That's why we need to apply a transformation to the point source data before running FWI.

After that, FWI tests for transformed data were performed. All inversions are run with the same parameter settings as used for the reference line source inversion. For the FWI result of transformed data using single velocity transformation, both dielectric permittivity and electrical conductivity models display artifacts in the upper part, hence, the shape of the trench cannot be defined. While, in the middle part, they show some interfaces parallel to the second interface in the model. In contrast, the FWI results of transformed data using reflected wave transformation show a better image. Two interfaces in the model can be recognized quite well. Although the bottom of the trench cannot be defined, the top can be delineated in the first layer in the dielectric permittivity model. There are more artifacts in the electrical conductivity models, hence, we cannot clearly define the shape of the trench. This is the same disadvantage compared to the FWI result of the line source, therefore, it should be considered as the cause of the FWI process, not because of the 3D-to-2D transformation.

Figure 3.14 displays a comparison of reference inversion and transformed data inversion. In which, the result of the reflected wave transformation shows a good matching with the reference inversion at small to medium offsets, especially for the reflected wave. From the 150th traces onward, the results of both transformations cannot fit with the reference inversion. As discussed above, this could be the contribution of the disadvantage of the FWI process, not only by the 3D-to-2D transformation.
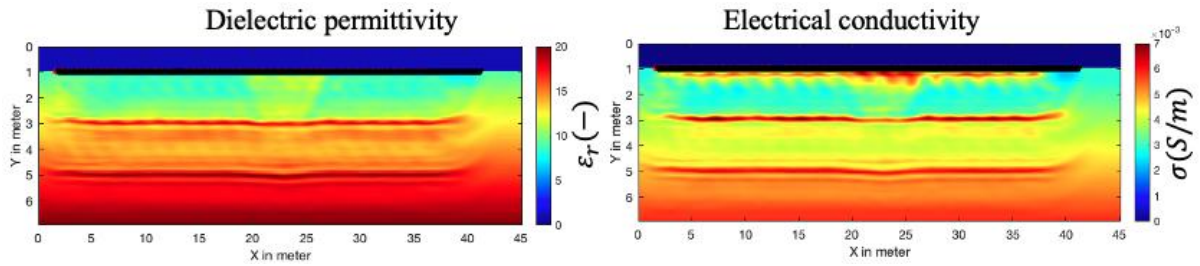
Figure 3.10 2D FWI result using perfect line source wavefields as observed data. Left model displays the dielectric permittivity model, right model is electrical conductivity.
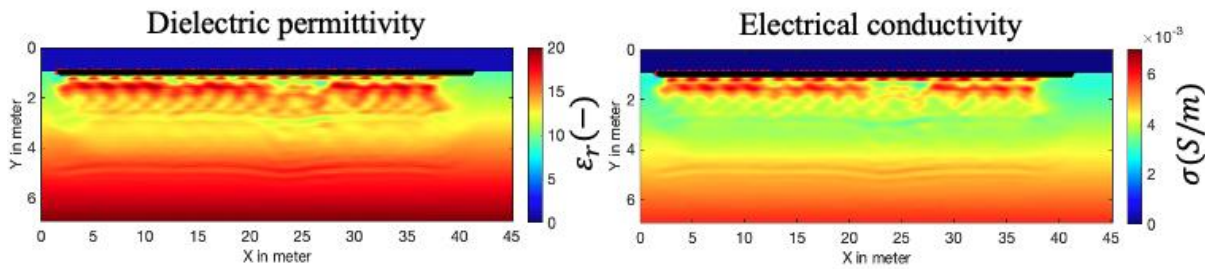

Figure 3.11 2D FWI result using point source wavefields as observed data. Left model displays the dielectric permittivity model, right model is electrical conductivity.
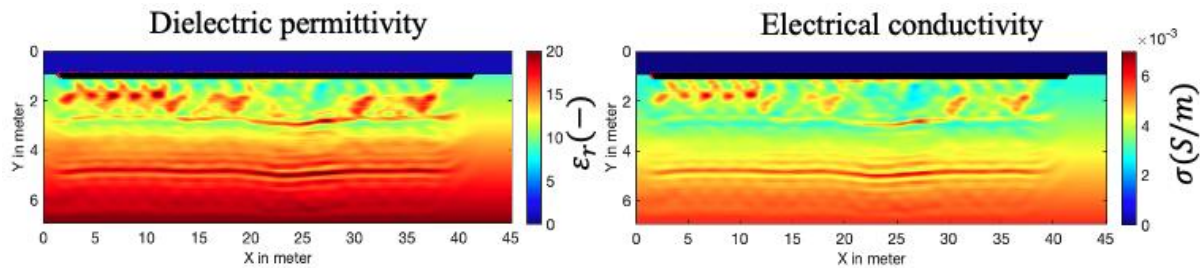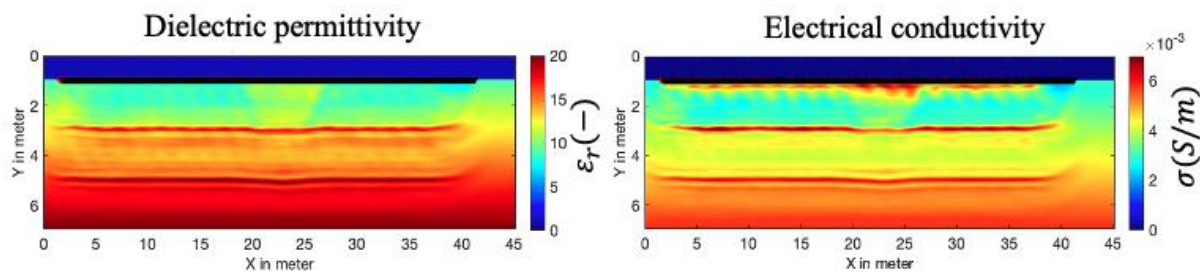

**Figure 3.12** 2D FWI result using transformed data of single velocity transformation as observed data. Left model displays the dielectric permittivity model, right model is electrical conductivity.

Figure 3.13 2D FWI result using transformed data of reflected wave transformation as observed data. Left model displays the dielectric permittivity model, right model is electrical conductivity.

23
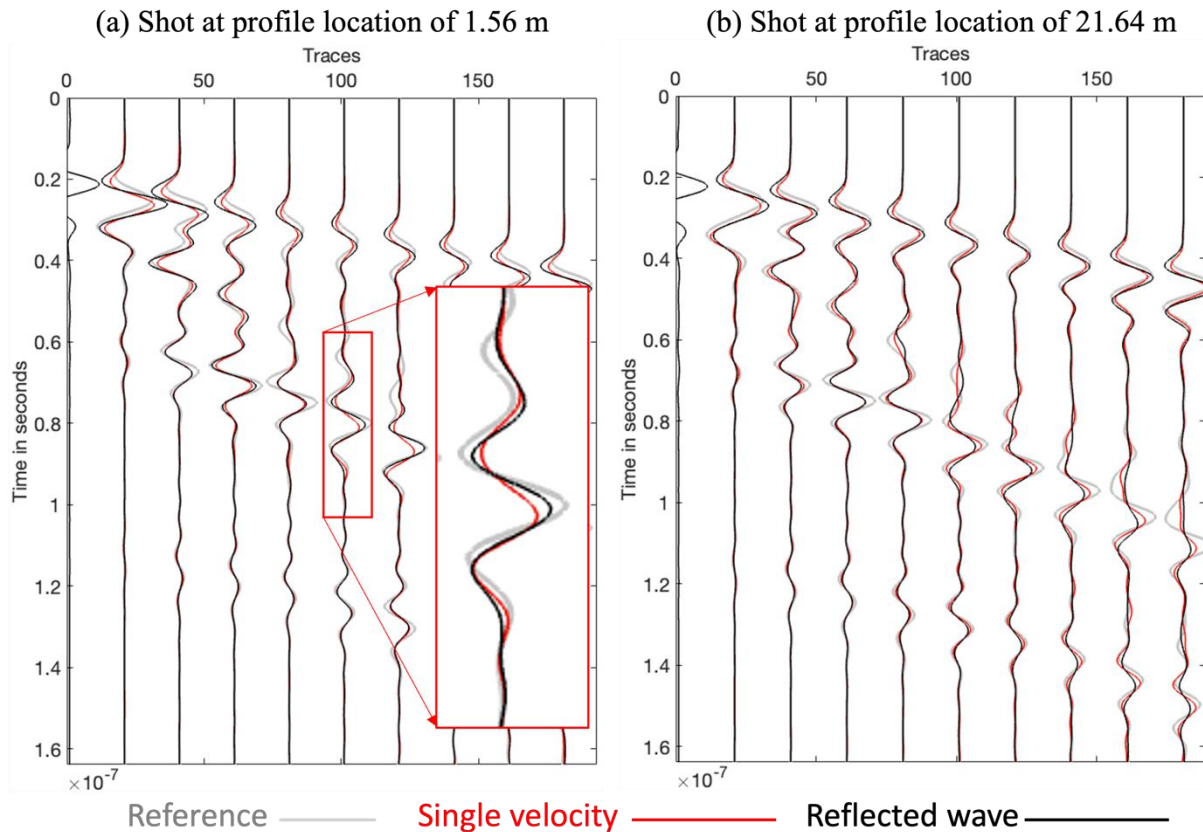
Figure 3.14 Comparison of FWI result of among line source radargrams, single velocity transformed radargrams and reflected wave transformed radargrams; only every 20th trace is displayed. Radargrams (a) show a shot at profile location of 1.56 m (very left-hand part of the model), radargrams (b) of 21.64 m (middle of the model). The radargrams are trace normalized to the amplitude scale of the reference inversion.

Summary

In this chapter, the different geometrical spreading of line source and point source wavefields has been studied by investigating the accuracy of the different numerical transformation techniques and by considering the matching of transformed point source data with the reference line source data. In order to apply this workflow to the field test site, synthetic models resembling the structure of the field data with a trench in the middle were generated. Subsequently, using the transformed point source radargrams in a 2D FWI as observed data, I investigated the artifacts introduced by the FWI process or by a line source simulation. In this study, although there are some residuals between the true line source data and the transformed data, the reconstruction of the transformed data using the reflected transformation can still delineate the main structure of the reference inversion. However, the values within these structures are not reliable. In addition, the FWI result of the electrical conductivity shows that this parameter is difficult to reconstruct compared to the dielectric permittivity. Reconstruction of the permittivity model proves to be more reliable, especially for defining the shape of anomalous objects when there's significant contrast with the surrounding environment.

The reconstructed permittivity model is more reliable and can be used to define the shape of an abnormal object if the contrast between it and the adjacent environment is large enough. Last but not least, using a proper 3D-to-2D transformation could help to get a better FWI result; in this case, the 3D-to-2D transformation of the reflected wave indicates a good result.

3.2. Field data

Setting

The field GPR data were acquired in the glider field in Rheinstetten, Germany. There are some previous studies in this area confirming the existence of a V-shaped trench so-called Ettlinger line, such as GPR migration imaging (Wegscheider, 2017) and shallow-seismic FWIs (Wittkamp et al., 2019; Gao et al., 2020; Pan et al., 2021; Irnaka et al., 2022), Indirect joint petrophysical Inversion of shallow seismic and GPR data (Qin, 2022). The target is a defensive trench which was first constructed in 1707 during the War of the Spanish Succession (Lang et al.,1907). It has been refilled and is no longer visible from the surface at the test site. The research area is in the glider field; therefore it is a flat area with no terrain. On the surface, there was a short layer of grass of about 10 cm at the time of the survey.
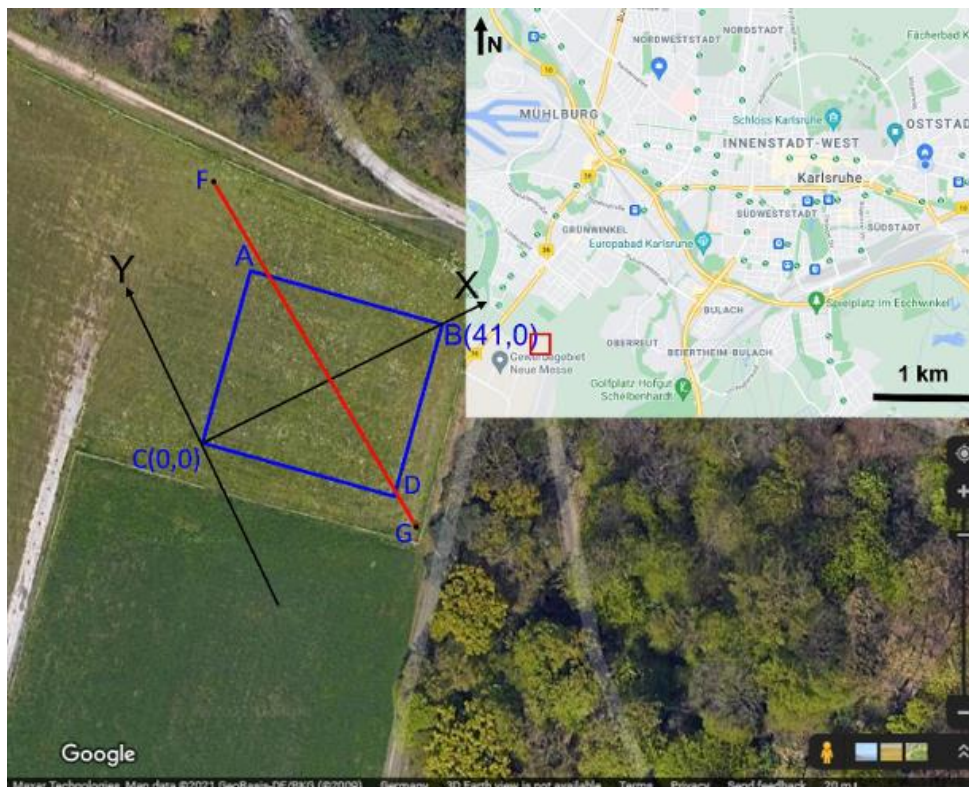

Figure 3.15 Overview map of the test site on the glider airfield in Rheinstetten. The red line corresponding to bottom of V-shape trench. The 2D FWI will be performed along CB line. Sources: Google map.

We acquired 165 multi-offset surface radargrams along a survey line CB (X-axis) perpendicular to the Ettlinger line that is presented as the red line FG in the Figure 3.15. We used an EKKO Pro pulse transmitter equipped with a pair of 200 MHz unshielded

25

antennas and a receiver mounted on a sledge for smooth movement. To track the receiver coordinates with an accuracy of less than a centimeter, we used real-time kinematic (RTK) positioning with a self-tracking total station (Boniger and Tronicke, 2010). Table 3.1 shows the setting of acquisition for the multi-offset surface GPR data.

Figure 3.16 shows the workflow of this section to deal with field data. In general, the workflow is the same as used for the synthetic data. For verification of the FWI results and the 3D-to-2D transformation, we have in situ data from boreholes at the field test site.

A data preprocessing workflow has been proposed by Qin, 2022. I will follow this workflow to preprocess field data before performing FWI. Table 3.2 summarizes the main workflow for data processing, in which, the data was resembled to the forward modelling requirement (Irving and Knight, 2006), and then the clipped amplitudes of high-energy direct arrivals that exceed the dynamic range of the acquisition unit are interpolated (Benedetto et al., 2017). In addition, low and high frequencies noises are also eliminated by direct current shift removal, dewow and band-pass filter. Then, we delete the traces with waveform distortions and remove the traces with an offset larger than 8 m. When acquiring data in the field, the trace spacing data is affected by the walking speed of the worker when moving the sled, and it was irregular speed. To ensure a balanced illumination in the measurement area, we apply the data gridding, i.e., 2D spline interpolation in the time-offset domain with regular trace spacing. Our forward engine uses a 2D forward modelling algorithm. As our field data can be assumed to spread from a point source and underlie 3D geometrical spreading, we have to apply the 3D-to-2D transformation to transform point source data to line source data. The 3D-to-2D transformation were used for the synthetic data test in the previous part will be applied to field data in this step.

Table 3.1 Settings of the acquisition of the GPR data at the Etllinger line test site and those used for FWI.

Parameters	Raw	FWI
Number of sources	165	18
Traces per gather	56~125	100~175
Transmitter spacing	~0.2 m	2 m
Receiver spacing	~0.1 m	0.04 m
Minimum offset	0.2 m	0.3 m
Maximum offset	17m	8 m
Sample rate	0.2 ns	0.08 ns
Recording window	200 ns	164 ns

Besides, I also used the same configuration for the inversion process as applied for the synthetic test presented in the previous part. In order to eliminate energy differences in

the data caused by the variation in instrument performance, antenna coupling or acquisition array, the gradient of each source is normalized before summation. Only 18 sources are used in the inversion to save computational cost. Figure 3.17 shows the initial models, which are set up as a gradual increase in relative dielectric permittivity from the ground at 9 to 14 at a depth of 6m. On the other hand, the initial electrical conductivity decreases from 3 mS/m to 1 mS/m.

Table 3.2 Multi-offset surface GPR data preprocessing steps

(1) Data resampling in the frequency domain
(2) Interpolation of clipped direct-arrival amplitudes
(3) DC-shift removal and dewow
(4) Bandpass filtering (5 – 400 MHz)
(5) Bad traces removal and offset limitation
(6) Data gridding in the time-offset domain
(7) 3D-to-2D transformation
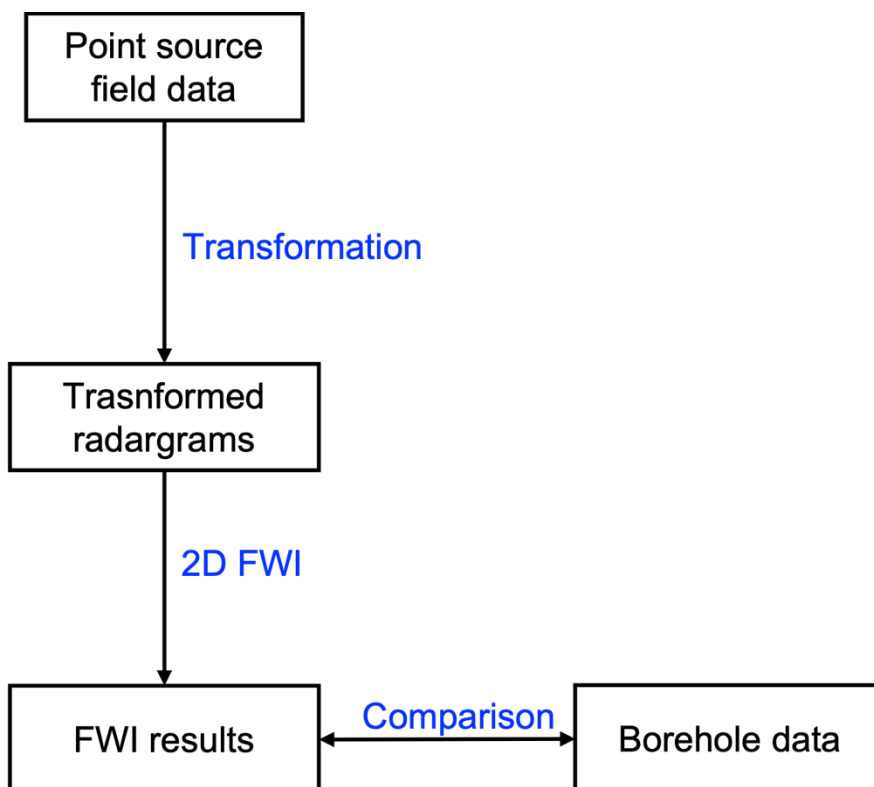
Figure 3.16 Workflow apply to the field data.
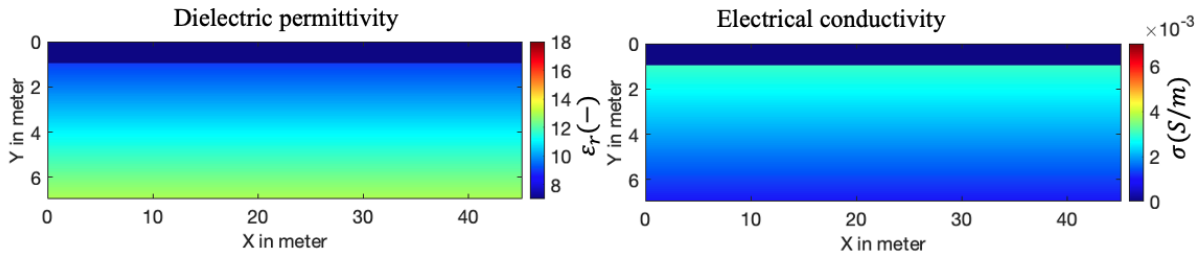
Figure 3.17 Initial model for reconstruction tests. Left model displays the dielectric permittivity model, right model is electrical conductivity.

Results

Figure 3.18 shows raw field data at two sources, where the first source (a) is located at the very left-hand part of the model and (b) is located in the middle of the model, which is estimated to be the location of the Ettlinger trench. In order to perform FWI , two 3D-to-2D transformations used in the synthetic test are applied to the field data. The amplitude factor of these transformations is shown in Figure 3.5.
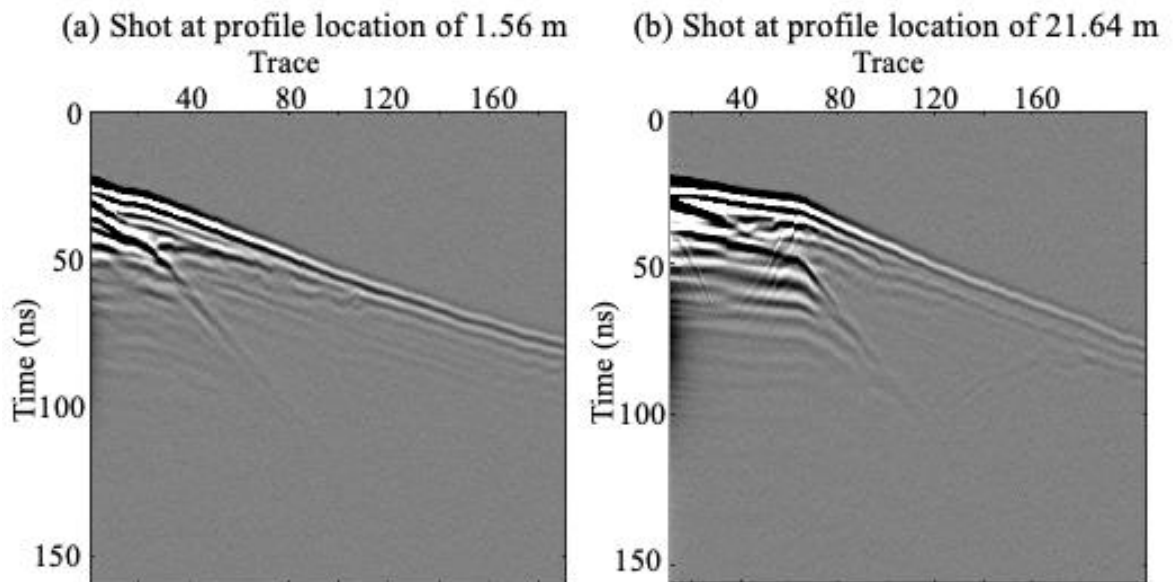
Figure 3.18 Field radargrams acquired in the field with a point source. Radargrams (a) show a shot at profile location 1.56 m (very left-hand part of the model), radargrams (b) of 21.64 m (middle of the model).

28
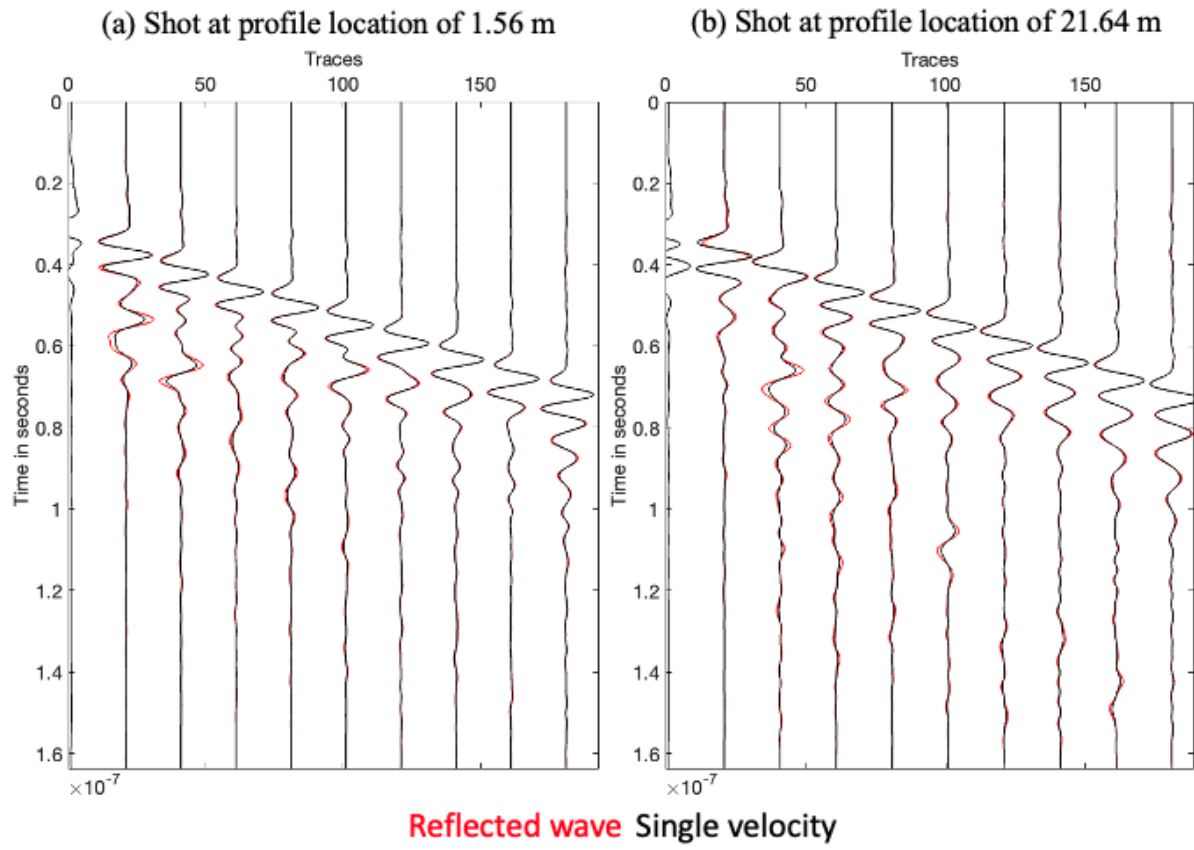
Figure 3.19 Comparison of result of single velocity transformed radargrams and reflected wave transformed radargrams; only every 20th trace is displayed. Radargrams (a) show a shot at profile location of 1.56 m (very left-hand part of the model), radargrams (b) of 21.64 m (middle of the model). The radargrams are trace normalized to the same scale.

Figure 3.19 display transformed data using single velocity transformation and reflected transformation. Since we are using the field data, we do not have a real line source data to make a comparison. However, according to the results from the synthetic test, the reflected wave transformation is expected to produce a better result of reconstruction of the field data.
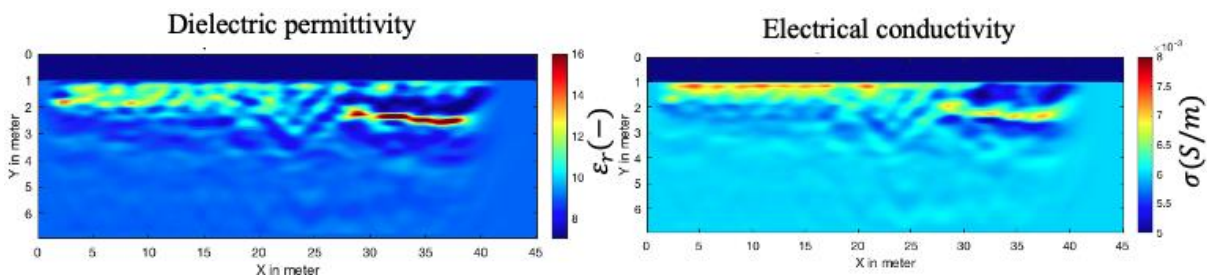
Figure 3.20 2D FWI result using transformed data of reflected wave transformation as observed data. Left model displays the dielectric permittivity model, right model is electrical conductivity.
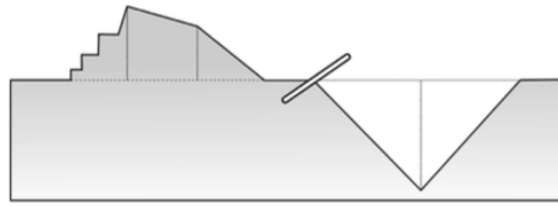
29

Figure 3.21 The original shape of the trench redraw from Lang et al. (1907)
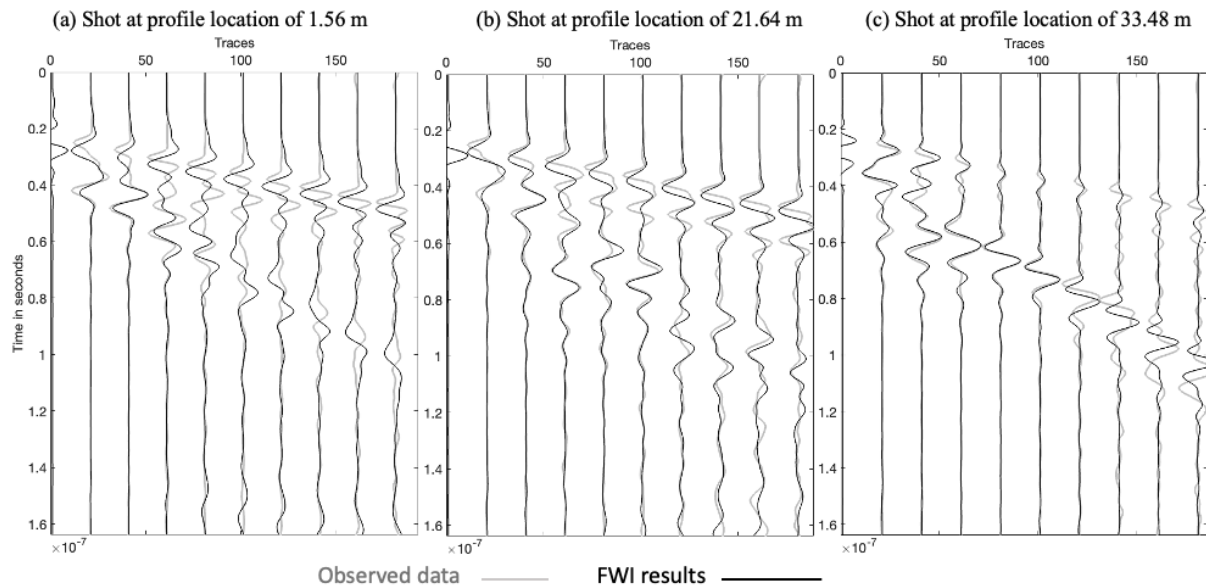

Figure 3.22 Result of FWI: comparison of reflected wave transformed data as observed data and its inversion results; only every 20th trace is displayed. Radargrams (a) show a shot at profile location of 1.56 m (very left-hand part of the model), radargrams (b) of 21.64 m (middle of the model) and radargram (c) of 33.48 m (very right part of the model). The radargrams are trace normalized to the amplitude scale of observed data.

As can be seen in Figure 3.20, an event extends from the right side of the model to the middle of the relative dielectric permittivity model. It could be interpreted as the interface of the expected trench. Due to the dielectric difference between the refilled sand and the underlying soil, this could be the interface between them, consistent with a weaker consolidation of the subsurface in the trench due to the excavation prior to backfilling (Irnaka et al., 2022). We do not see this event on the left side of the model which is quite consistent with the schematic model of Irnaka (2022) that is shown in Figure 3.21. Instead, a layer of high conductivity is seen on this side. This could be the reason for a significant amplitude attenuation of the ground waves and reflected waves on the radargram at location 1.56 m (Figure 3.22a). Besides, there is a strong reflector on the right side of the trench at around 1 m depth indicating a large contrast between the upper and lower trench surface. This reflector was clearly visible on the radargram at location of 33.48m (Figure 3.22c). However, similar to our observation in the synthetic examples, the absolute values of permittivity inside the trench are less reliable because the surface GPR data lack low wavenumber information. The strong reflector still appears in the electrical conductivity model, and although it is not as clear as in the

relative permittivity model, we can still see the bottom of the trend. When comparing the observed data and the FWI results of this inversion, similar to the synthetic data test, the reflected wave shows a good fitting at small to medium offset of reflected wave (Figure 3.22). In this case, these differences are due to both the disadvantage of FWI process and the 3D-to-2D transformation.

Another 2D FWI was also performed on the transformed single velocity data, as shown in Figure 3.23. Although we can delineate the bottom of the trench in the resulting models, the same drawbacks of this transformation still occur in the field data when there are more artifacts in the upper part of both models. The artifact in the lower part, which was also present in the result of FWI using the reflected wave (Figure 3.20), is more pronounced in this result. In all data, both in the Figure 3.22 and Figure 3.24, the air and ground waves are not match with the observed data due to using the 3D-to-2D transformation of the reflected wave and the single velocity. Furthermore, the forward solver employed in this investigation lacks the ability to account for the radiation pattern and correct antenna coupling as they occur in real-world scenarios (Qin, 2022).
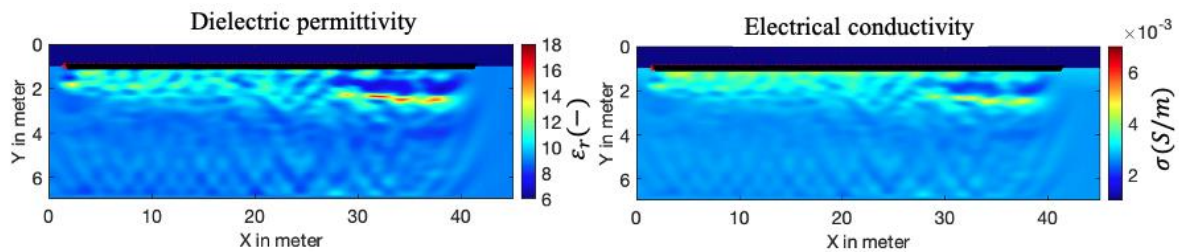

Figure 3.23 2D FWI result using transformed data of single velocity transformation as observed data. Left model displays the dielectric permittivity model, right model is electrical conductivity.
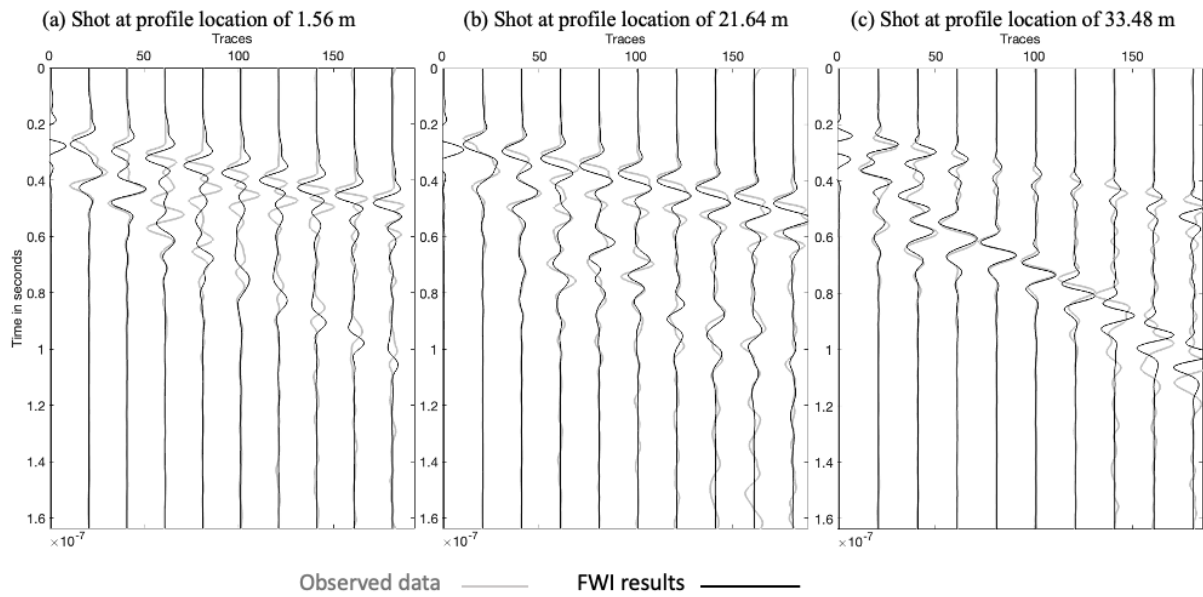
Figure 3.24 Result of FWI: comparison of single velocity transformed data as observed data and its inversion results; only every 20th trace is displayed. Radargrams (a) show a shot at profile location of 1.56 m (very left-hand part of the model), radargrams (b) of 21.64 m (middle of the model) and radargram (c) of 33.48 m (very right part of the model). The radargrams are trace normalized to the amplitude scale of observed data.

4. Comparison to borehole data

In addition to the acquiring GPR data along this profile, our fieldwork included the drilling of boreholes, strategically positioned to complement the geophysical survey data. Boreholes BH2, and BH3 were drilled concurrently with the multi-offset surface GPR measurements, providing a direct correlation between the GPR data and the subsurface conditions at those specific points. However, boreholes BH4 and BH7 were drilled in the study area one year after the initial GPR survey. Soil samples were taken at every 50 cm. At specific points where significantly changing in properties, soil samples interval was reduce to 25 cm.

To compare FWI results and borehole data, we need to convert them to the same parameter. In this case, I will convert the measured water content of the borehole data to dielectric permittivity to compare with that of the FWI result. We know that the dielectric permittivity depends on several factors such as water content, mineralogy, grain size, and bulk density of the material, but if only general algorithms are used to determine these relationships, it carries significant inaccuracies (up to 200% error for clay substrates) (Owenier et al., 2011). They introduced empirical equations describing the relationship between relative permittivity and water content (Table 4.1) based on grain size and composition of the materials . As shown in Figure 4.1, for the same dielectric permittivity value, there are many different water content values, therefore, it is necessary to measure the grain size of the soil sample to define a proper relationship.
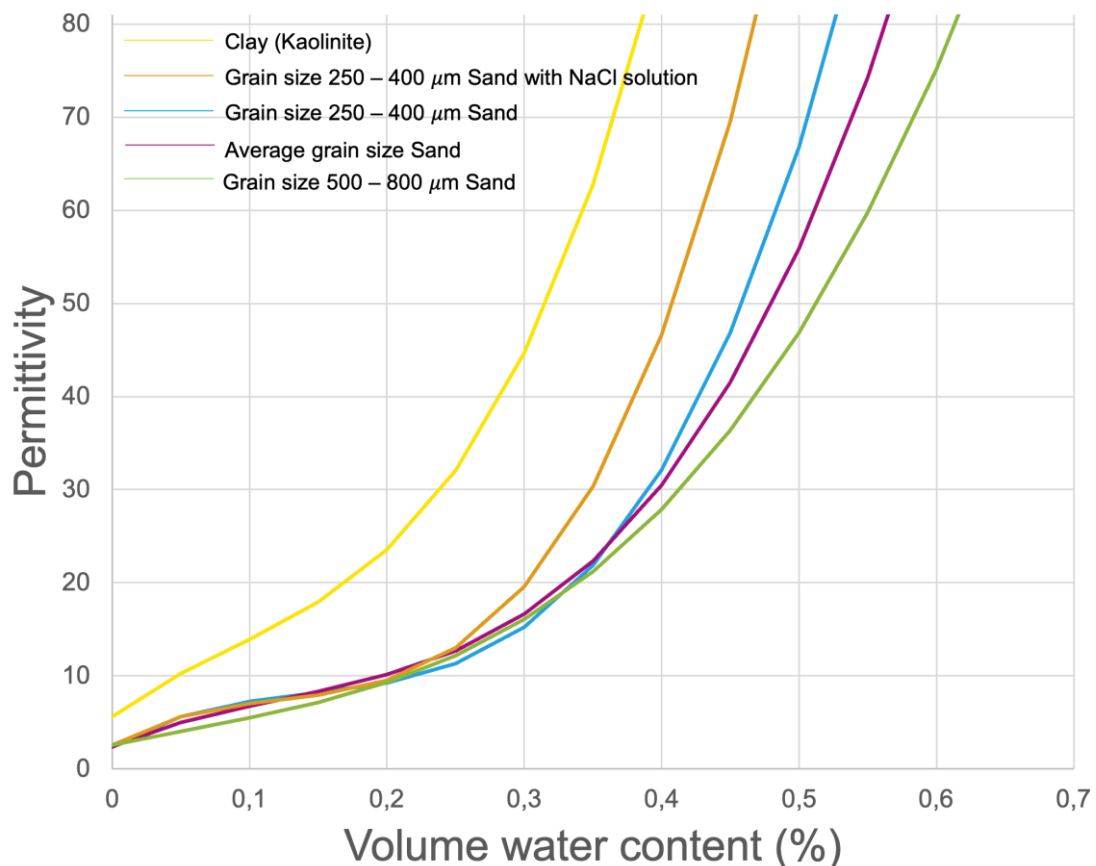

Figure 4.1   Different relations between dielectric permittivity and volume water content (Owenier et al., 2011).

33

Table 4.1 Empirical equations between soil moisture and relative permittivity (ε) for different materials; measurements at 200MHz (Owenier et al., 2011).

Material	Empirical equations
Sand grain size 250-400 µm	$\varepsilon = 2{,}36 + 86{,}9\,\theta - 492{,}84\,\theta^2 + 1153{,}7\,\theta^3$
Sand grain size 500-800 µm	$\varepsilon = 2{,}57 + 31{,}9\,\theta + 61{,}7\,\theta^2 + 350{,}3\,\theta^3$
Sand gain size 250-400 µm with NaCl solution	$\varepsilon = 259 + 85{,}2\,\theta - 567{,}8\,\theta^2 + 1575\,\theta^3$
Kaolinite (25-35 µm	$\varepsilon = 5{,}63 + 110{,}9\,\theta - 447{,}8\,\theta^2 + 1707\,\theta^3$
Sand Average	$\varepsilon = 2{,}39 + 63\,\theta - 262\,\theta^2 + 700\,\theta^3$

When analyzing the grain size distribution of the collected soil samples, the timing of the borehole drilling, whether done simultaneously with the GPR measurements or a year later, does not affect the grain size results. Soil composition is generally stable over short periods of time unless the site is subject to significant erosion, sediment deposition or human activity that could drastically alter the soil composition. Therefore, samples from all boreholes are valuable in assessing the subsurface grain size distribution and providing a comprehensive understanding of the physical properties of the soil through the profile.

However, the situation is different for soil water content measurements. Samples from boreholes BH4 and BH7, drilled one year later, could not be reliably used for water content measurements. This limitation arises because soil water content is highly variable and influenced by a variety of factors including seasonal changes, precipitation patterns, and human activities such as irrigation or drainage. The lapse of a year between sample collection means that the later samples may not accurately reflect the conditions present at the time of the initial GPR survey and the drilling of the first three boreholes. Consequently, any attempt to correlate the water content measurements from the later boreholes with the GPR data collected a year earlier would likely yield misleading conclusions about the subsurface conditions at the time of the survey.

Figure 4.3 shows the results of grain size measurements for BH4 and BH7. The colors indicate the grain size of the samples at different depths. Although the grain size measurement results for two boreholes are different, both show a wide range of grain size distribution, from smaller than 200 μm to over 500 μm.
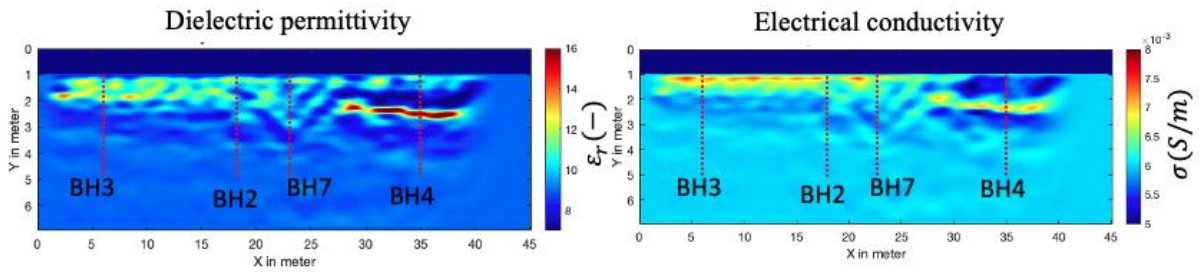
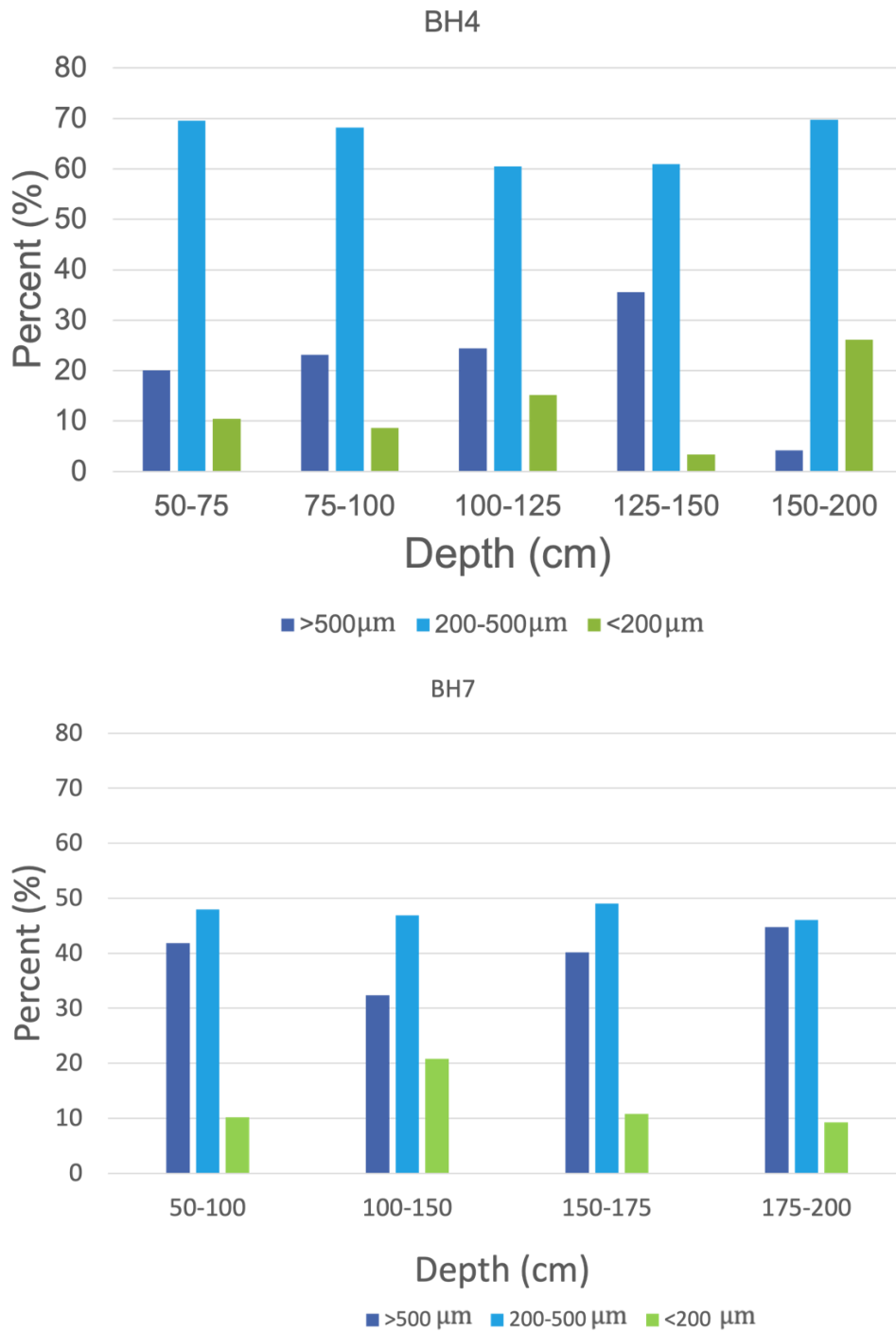**Figure 4.2** Location of boreholes in the models.

Figure 4.3 Grain size distribution curves at two boreholes.

Soil sample of BH2, BH3 were used to measure water content by Qin (2022). Figure 4.4 shows the results of this measurement. Following the empirical equation between soil moisture and effective relative permittivity (ε_{er}) for different materials; measurements at 200MHz, we can calculate the relative permittivity from the result of water content measurement. There are five equations for sand with different grain sizes (Table 4.1). Based on the grain size measurement result above, the equation for sand average might be appropriate for our samples. In addition, to compare with the calculated relative permittivity, FWI results using reflected wave transformed data for relative dielectric permittivity are extracted at borehole locations. However, since the results of GPR FWI below 3m are not reliable, we compare only the shallow part (≤3m) in Figures 4.5 and 4.6. In the following, I refer to the relative permittivity of the FWI result as the extracted permittivity and that calculated from the water content as the calculated permittivity.
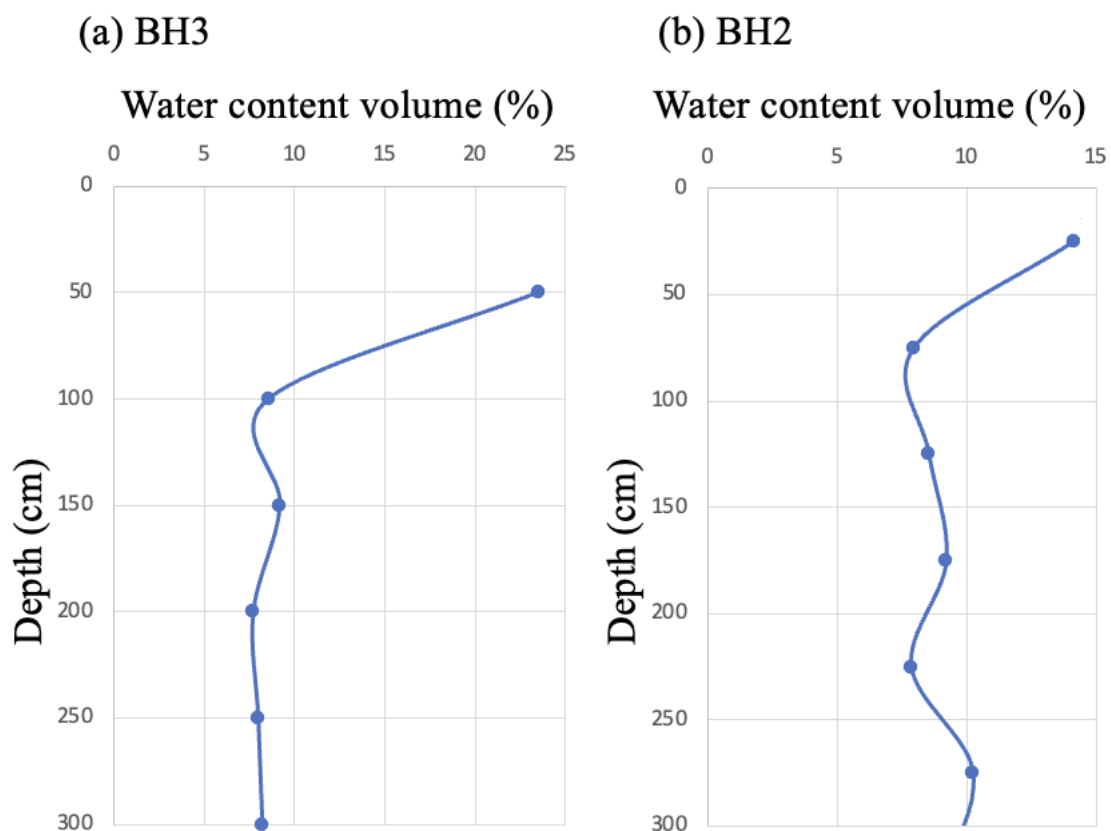

Figure 4.4 Water content volume results at boreholes.

A notable discrepancy is observed in the extracted permittivity values at a depth of 0.75 m at borehole BH3. This may correspond to the high conductivity anomaly layer observed in the dielectric model presented in Figure 4.2. However, the calculated permittivity curve derived from borehole data is unable to define this layer. A similar phenomenon was observed at BH2 at a depth of approximately 0.75 m. This discrepancy may be attributed to the limited number of borehole samples, which results in disparate resolutions between the FWI result and the calculated results from borehole samples. Consequently, a detailed comparison between the two data sets is not feasible.

Furthermore, a bias is observed between the calculated data and the FWI result in both boreholes. It is possible that this discrepancy is attributable to an error in the measurement of water content or lacking long wavelength information in the surface multi-offset GPR data.

Notwithstanding these discrepancies, the overall pattern remains consistent. At BH3, two curves commence with a high permittivity value at the surface, which then decreases sharply at a depth of approximately 1 m, followed by minor fluctuations throughout the remaining depth. Similarly, in Figure 4.6, aside from the anomaly at approximately 0.75 m depth, it is observed that the two lines run parallel to each other, with a decrease in value for the top 75 cm, followed by a slight increase and decrease for the lower part.
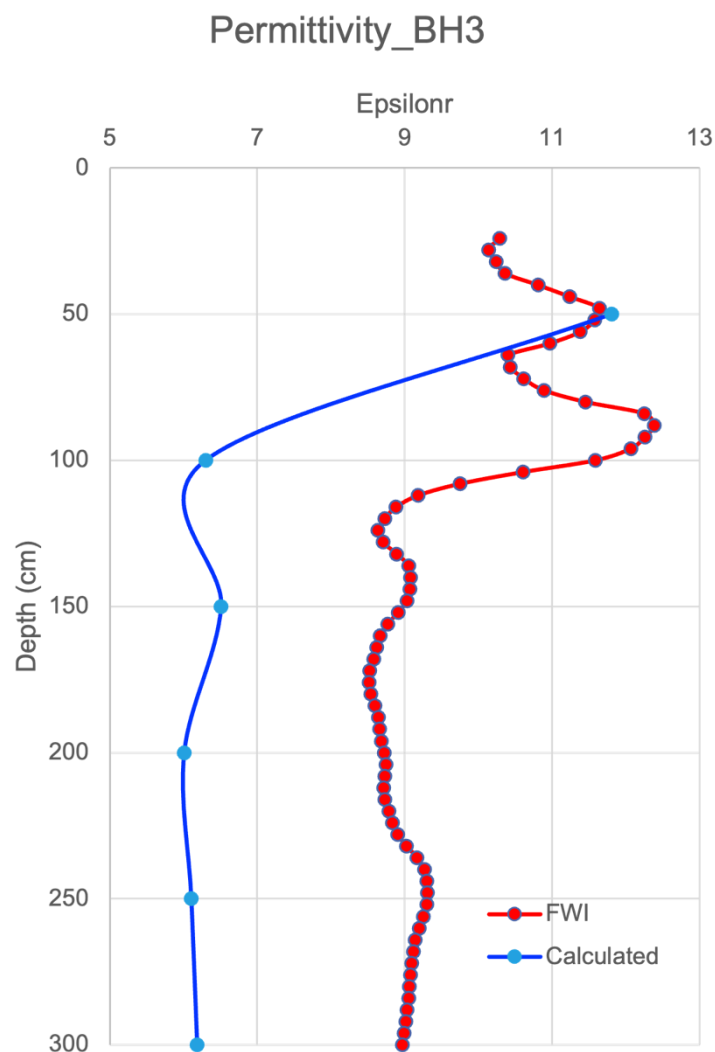

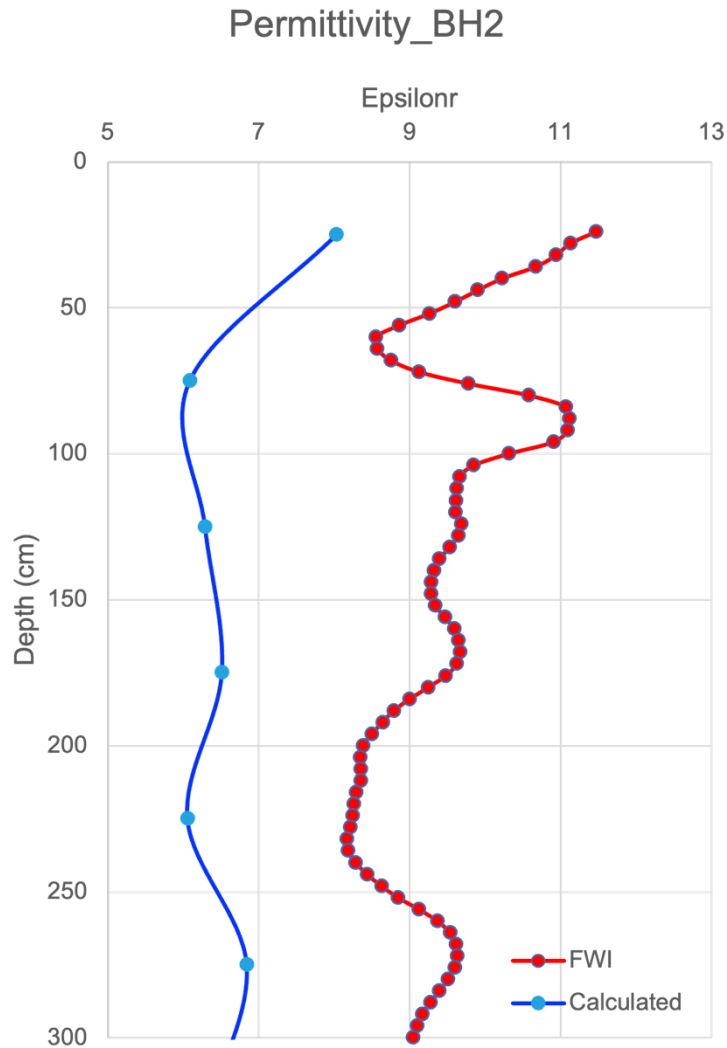**Figure 4.5** Comparison dielectric permittivity of FWI result and calculated from water content at BH3 location.

Figure 4.6 Comparison dielectric permittivity of FWI result and calculated from water content at BH2 location.

Summary

Based on the grain size measurement, an optimal relation between permittivity (FWI result) and water content (borehole data) was selected for this study area. A comparison between the FWI results and the borehole data indicates a similar trend. However, due to the limited number of borehole samples, a detailed comparison is not possible. Moreover, there is a bias between the absolute values of the two data sets due to the lack of long wavelength information in the surface multi-offset GPR data and the system error when measuring water content.

38

5. Conclusion

In this study, I investigate the performance of the 3D-to-2D transformation of different waves for multi-offset surface GPR data, and its effect on the result of 2D GPR-FWI. By considering the differences in velocity and phase between waves when transforming data generated by point sources to those generated by line sources, different sets of transformed data were obtained. The effectiveness of the 3D-to-2D transformation of the reflected wave was confirmed by the similarity between the transformed data and the 2D reference data. As a consequence, using the reflected wave transformed data as observed data in 2D GPR-FWI produces comparable results to those using 2D data as observed data.

When applied to field data acquired at the Rheinstetten test site in Germany, where the existence of a refilled trench was confirmed by previous studies, the results of the multi-offset 2D GPR-FWI show anomalous triangular features in the relative dielectric permittivity and electrical conductivity models. These features are situated in the middle of the 2D line and potentially indicate the presence of the historically buried trench.

Additionally, the results of the 2D GPR-FWI are then evaluated by comparing the relative dielectric permittivity values to those calculated from in borehole data at the borehole locations. The results show a similar trend with respect to depth, proving that the reconstructed models from 2D GPR-FWI using the result of the 3D-to-2D transformation of the reflected wave are similar to the borehole data.

To further improve the 3D-to-2D transformation, we could separately transform data for each wave type in the tau-pi domain, and then combine them to obtain a comprehensive result for different waves. However, the actual performance of this transformation requires further study to assess its efficiency.

Bibliography

Bai, W., Kong, L., Guo, A. (2013). Effects of physical properties on electrical conductivity of compacted lateritic soil. *Journal of Rock Mechanics and Geotechnical Engineering*, 5(5): 406-411. https://doi.org/10.1016/j.jrmge.2013.07.003.

Berard, B. A., Maillol, J. (2007). Multi-offset ground penetrating radar data for improved imaging in areas of lateral complexity — Application at a Native American site. *Journal of Applied Geophysics*, 62(2): 167-177. https://doi.org/10.1016/j.jappgeo.2006.10.002.

Bleistein, N. (1986). Two-and-one-half dimensional in-plane wave propaga- tion, *Geophysical Prospetcing,* 34: 686–703. https://doi.org/10.1111/j.1365-2478.1986.tb00488.x

Boniger, U., Tronicke, J. (2010). On the potential of kinematic GPR surveying using a self-tracking total station: Evaluating system crosstalk and latency. *IEEE Transactions on Geoscience and Remote Sensing*, 48(10):3792–3798. http://doi.org/10.1109/TGRS.2010.2048332

Bunks, C., Saleck, F. M., Zaleski, S., Chavent, G. (1995). Multiscale seismic waveform inversion. *Geophysics,* 60(5): 1457–1473. https://doi.org/10.1190/1.1443880

Carcione, J. M. (1996). Ground-penetrating radar: Wave theory and numerical simulation in lossy anisotropic media. *Geophysics*, 61(6):1664–1677. https://doi.org/10.1190/1.1444085

Dampney, C. N. G. (1971). The relationship between two- and three-dimensional elastic-wave propagation, *Bull. seism. Soc. Am*., 61(6): 1583–1588. https://doi.org/10.1785/BSSA0610061583

Forbriger, T., Groos, L., Schäfer, M. (2014). Line-source simulation for shallow-seismic data. Part 1: theoretical background. *Geophysical Journal International,* 198(3): 1387-1404. https://doi.org/10.1093/gji/ggu199

Gao, L., Pan, Y., Bohlen, T. (2020). 2-D multiparameter viscoelastic shallow-seismic full-waveform inversion: reconstruction tests and first field-data application. *Geophysical Journal International*, 222(1):560–571. https://doi.org/10.1093/gji/ggaa198

Gomaa, M. M. (2022). Grain size effect on electrical properties of dry friable sand. *Eur. Phys. J. Spec. Top.* https://doi.org/10.1140/epjs/s11734-022-00667-7

Hossain, M. S., Islam, M. A., Badhon, F. F., Imtiaz, T. (2021). Properties and Behavior of Soil - Online Lab Manual, Chapter 3. *Mavs Open Press*, ISBN: 978-1-64816-971-7.

Irnaka, T. M., Brossier, R., Métivier, L., Bohlen, T., Pan, Y. (2022). 3-D multicomponent full waveform inversion for shallow-seismic target: Ettlingen Line case study, *Geophysical Journal International*, 229(2):1017–1040. https://doi.org/10.1093/gji/ggab512

Klotzsche, A., Vereecken, H., Kruk, J. V. D. (2019). Review of crosshole ground-penetrating radar full-waveform inversion of experimental data: Recent developments, challenges, and pitfalls. *Geophysics*, 84(6):1ND3–Z34. https://doi.org/10.1190/geo2018-0597.1

Lang, K., 1907. Die Ettlinger Linien und ihre Geschichte*, G. Braunschen Hofbuchdruckerei.* Available at: https://archive.org/details/dieettlingerlini00lang_0

Lavoué, F. (2014). 2D full waveform inversion of ground penetrating radar data: towards multiparameter imaging from surface data. PhD thesis, *Université de Grenoble*. Available at: https://theses.hal.science/tel-01551800/document

Lombardi, F., Podd, F., Solla, M. (2022). From Its Core to the Niche: Insights from GPR Applications. *Remote Sens,* 14(13): 3033. https://doi.org/10.3390/rs14133033

Owenier, F., Hornung, J. & Hinderer, M. (2011): Dielectric permittivity of geologic Materials at different water contents - Measurements with an impedance analyzer, *6th International Workshop on Advanced Ground-penetrating radar (IWAGPR)*, Aaachen, Germany,1-5. http://doi.org/10.1109/IWAGPR.2011.5963836.

Pan, Y., Gao, L., Bohlen, T. (2021). Random-objective waveform inversion of 3D-9C shallow seismic field data. *Journal of Geophysical Research: Solid Earth*, 126(9): e2021JB022036. https://doi.org/10.1029/2021JB022036

Paz, C., Alcalá, F. J., Carvalho, J. M., and Ribeiro, L. (2017). Current uses of ground-penetrating radar in groundwater-dependent ecosystems research. *Science of the Total Environment*, 595:868–885. https://doi.org/10.1016/j.scitotenv.2017.03.210

Plessix, R. E., Mulder, W. (2004). Frequency-domain finite-difference amplitude-preserving migration. *Geophysical Journal International*, 157(3):975–987. https://doi.org/10.1111/j.1365-246X.2004.02282.x

Plessix, R. E. (2006), A review of the adjoint-state method for computing the gradient of a functional with geophysical applications. *Geophysical Journal International*, 167: 495-503. https://doi.org/10.1111/j.1365-246X.2006.02978.x

Polak, E. and Ribiere, G. (1969). Note on convergence of conjugate direction methods. *Revue Francaise D Informatique De Recherche Operationnelle*, 3(16):35–43. Available at: http://www.numdam.org/item/M2AN_1969__3_1_35_0/

Qin, T., Bohlen, T., Allroggen, N. (2013). Full-waveform inversion of ground-penetrating radar data in frequency-dependent media involving permittivity attenuation, *Geophysical Journal International*, 232(1): 504–522. https://doi.org/10.1093/gji/ggac319

Sato, M. (2001). GPR and Its Application to Environment Study, *Seminar of Geology, Geophysics, Hydro-geology, Archaeology, Civil Engineering at Mongolian Technical University, Ulaanbaatar, Mongolia*. Available at: https://www.researchgate.net/publication/229006463_GPR_and_Its_Application_to_Environmental_Study

Schafer, M., Groos, L., Forbriger, T., Bohlen, T. (2014). Line-source simulation for shallow-seismic data. Part 2: Full-waveform inversion-a synthetic 2-D case study. *Geophysical Journal International*. 198(3), 1405-1418. https://doi.org/10.1093/gji/ggu171

Topp, G.C., Davis, J.L., Annan, A.P. (1980) Electromagnetic Determination of Soil Water Content: Measurements in Coaxial Transmission Lines. *Water Resources Research*, 16(3): 574-582. https://doi.org/10.1029/WR016i003p00574

Ursin, B., (1990). Offset-dependent geometrical spreading in a layered medium. *Geophysics*. 55: 492-496. https://doi.org/10.1190/1.1442860

Wegscheider, S. (2017). Abbildung der Ettlinger Linie auf dem segelflugplatz Rheinstetten mittels Georadars [Illustration of the Ettlinger line on the gliding airfield Rheinstetten by means of GPR]. Master's thesis, *Karlsruhe Institute of Technology*. Available at: https://publikationen.bibliothek.kit.edu/1000152587/149693500

Wittkamp, F., Athanasopoulos, N., and Bohlen, T. (2019). Individual and joint 2-D elastic full-waveform inversion of Rayleigh and Love waves. *Geophysical Journal International,* 216(1):350–364. https://doi.org/10.1093/gji/ggy432

Yang, P., Brossier, R., Métivier, L., Virieux, J. (2016). A review on the system- atic formulation of 3-D multiparameter full waveform inversion in viscoelastic medium. *Geophysical   Journal   International*,   212(3):1694–1695. https://doi.org/10.1093/gji/ggx493

Acknowledgements